Industrial Chemistry & Materials

ROYAL SOCIETY OF CHEMISTRY

PAPER

View Article Online
View Journal

Cite this: DOI: 10.1039/d5im00372e

Sub-millibar pressure gradient along a gravity-driven percolated CO_2 gas diffusion electrode for vertical scale-up

Craig Armstrong, [a] Bjørnar Sandnes [b] and Enrico Andreoli *[a]

Herein the operating principles of a carbon dioxide electrolyser employing a percolator material and a gravity-fed electrolyte are demonstrated. By precisely adjusting reservoir elevations, the catholyte pressure profile applied to the CO_2 gas diffusion electrode as a function of height is deliberately manipulated. This approach enables the control of pressure differentials across the entire electrode, and the mitigation of hydrostatic pressure accumulation within the catholyte which would otherwise exceed the limited pressure resilience of present electrodes. To rationalise the fluid physics of operation, a tractable model that predicts the internal pressure profile within the percolator was developed, requiring only simple reservoir height adjustments to account for head losses specific to the electrolyser architecture. To validate and apply this model, a 32 cm tall electrolyser with vertical differential pressure monitoring was employed, demonstrating sub-millibar pressure gradients during operation. Under these conditions, stable CO_2 electrolysis was achieved, demonstrating the prospect of vertically scaled systems which is critical for industrial implementation.

Keywords: Falling film electrolyser (FFE); Electrochemical carbon dioxide reduction (EC-CO_2R); Gas diffusion electrodes (GDEs); Differential pressure; Vertical scale-up; Stability.

Received 12th December 2025,
Accepted 13th February 2026

DOI: 10.1039/d5im00372e

rsc.li/icm

1 Introduction

The urgency of climate mitigation is reshaping the foundations of global energy and industry, calling for transformative changes beyond incremental efficiency gains.[1] The transition of the chemical industry towards defossilisation and electrification is pivotal for achieving a sustainable and circular economy. While traditionally reliant on fossil-derived feedstocks, the sector is now exploring innovative pathways to reduce its carbon footprint.[2] One promising approach involves utilising CO_2 emissions from hard-to-abate industries, such as steel and cement production, as a carbon alternative for synthesising valuable chemicals and fuels. This integration not only mitigates emissions from these sectors but also provides a renewable carbon source for chemical manufacturing.[3] Electrochemical carbon dioxide reduction (EC-CO_2R) has emerged as a key technology that offers the direct conversion of captured CO_2 into a range of chemicals and fuels using renewable electricity.[3–5] Operating at low temperature and pressure, and using sustainable environmental materials, the scale-up of EC-CO_2R holds great promise for tailored and modular electrified CO_2 recycling.[6–9] Notably, systems operating at industrially relevant current densities and selectivity have been demonstrated, with continued progress needed to move the technology closer to commercial viability.[4,10–12]

From a chemistry perspective, CO_2 is effectively inert under ambient conditions, thus the prevailing problems with CO_2 electrocatalysis are well documented in terms of reaction selectivity and efficiency. Yet significant progress has been made *via* finesse control of catalyst composition, morphology, and nano-structuring to demonstrate high faradaic efficiencies.[13–17] For example, Chen *et al.* demonstrated 87% ethylene using a polyamine-incorporated Cu catalyst in 2020.[18,19] Typically, catalysis advancements are achieved in small-scale experiments and often employing planar electrodes, but translating these achievements into scalable electrolysers is problematic due to limited conversion rates,[20] low energy/carbon efficiency,[21] selectivity loss and electrode instability.[22] Furthermore, technological economic assessments frequently project that consistent current densities above 100 mA cm^{-2}, low cell voltages below 2 V and lifetimes of several years are required for feasibility.[23–26] Planar electrodes fail to meet this requirement

[a] *SUSTAIN – Future Steel Manufacturing Research Hub, Department of Chemical Engineering, Faculty of Science and Engineering, Swansea University, Swansea, SA1 8EN, UK. E-mail: e.andreoli@swansea.ac.uk*
[b] *Complex Fluids Research Group, Department of Chemical Engineering, Faculty of Science and Engineering, Swansea University, Swansea, SA1 8EN, UK*

due to insufficient CO_2 mass transport arising from the low ~33 mM solubility limit of CO_2 dissolved in water.[27,28] In contrast, gas-fed reactors realise much faster conversion rates due to the vastly higher CO_2 concentration supplied to the catalyst and the compression of the interface diffusion layer to the nanoscale.[20] Consequently, economically viable current densities have been regularly demonstrated in the literature, with partial current densities exceeding 300 mA cm^{-2} for large hydrocarbons such as ethanol production.[29] However, this high performance is often accompanied by stability loss and limited lifetimes, with reports of multi-day operation for hydrocarbon production being rare.[22]

A key component in operating gas-fed reactors is the gas diffusion electrode (GDE) employed for the cathodic EC-CO_2R process.[27,30] The GDE must function as a barrier between the CO_2 and electrolyte compartments of the electrolyser, whilst being permeable to gaseous CO_2 and product diffusion to/from the catalyst. In addition, the GDE must be electrically conductive and electrochemically inert to avoid side reactions or corrosion. Thus, the design considerations of GDEs are highly demanding and somewhat at odds with each other. CO_2 mass transport optimisation favours minimised diffusion path lengths and thinner GDEs, whereas electrolyte repulsion is enhanced by thicker materials with smaller pores.[31] Presently, commercial GDEs for EC-CO_2R do not exist, so gas diffusion layers (GDLs) from the highly developed fuel cell technology are routinely applied in EC-CO_2R research instead.[32] These GDLs are conventionally carbon-based and consist of two layers; a macroporous carbon fibre substrate (CS) with a thickness of ~250 μm,[33,34] and a thinner microporous layer (MPL) of ~50 μm[33,34] composed of fine carbon powder and polytetrafluoroethylene (PTFE). A fine catalyst layer (CL) (typically ~5 μm thick with loadings in the range of 0.1 to 2.0 mg cm^{-2}) is then coated onto the MPL composed of nanoparticles for enhanced surface area and activity, along with ionomer serving as a proton conductor and binder.[33,35]

Fundamentally, GDEs exploit three-phase boundaries where CO_2 gas, aqueous electrolyte, and conductive catalyst surfaces converge to enable proton-coupled electron transfers to adsorbed CO_2.[28] The configuration of these boundary interfaces is therefore critical to operation and is maintained by the GDL hydrophobicity which repels the electrolyte.[36] Unfortunately prolonged GDE operation causes the electrolyte to penetrate beyond the catalyst layer resulting in adverse performance,[37,38] and eventually the flooding of the CO_2 chamber.[39,40] Known as 'electro-wetting', a shift towards parasitic hydrogen evolution is observed driven by a combination of exposed electroactive carbon and a fully wetted catalyst leading to a large CO_2 depletion layer.[40,41] In addition, electrolyte penetration may also be driven by 'pressure-wetting' whereby excessive electrolyte pressure overcomes the threshold capillary pressure of the porous material.[42] GDEs therefore require a subtle and meticulous pressure balance between CO_2 and electrolyte to be maintained across the entire electrode surface. Whilst trivial at the centimetre laboratory scale, pressure balance becomes problematic at the industrial multi-metre scale because the pressure of a conventionally pumped electrolyte accumulates as a function of depth due to gravity. With current GDEs possessing a low pressure resilience of typically <100 millibar differential (mbarD),[33] the practical height of a pumped EC-CO_2R electrolyser is therefore limited.

Evidently, an alternative approach to conventional pumping is required to better regulate the electrolyte pressure and achieve a vertically uniform pressure distribution. This challenge was previously addressed during the development of modern chlor-alkali electrolysers employing 'oxygen depolarised cathodes' (ODCs).[43] Chlor-alkali electrolysis is an industrial scale process whereby chlorine gas is produced in tandem with sodium hydroxide in an aqueous electrolytic cell featuring a cation exchange membrane. Initial chlor-alkali electrolysers were inefficient due to the water-splitting cathode employed, however the development of the ODC, whereby oxygen gas is reduced, depolarised the cell voltage by 1.23 V and reduced energy consumption by 30%.[44] The ODC is essentially an oxygen GDE and directly analogous to CO_2 GDEs used presently. In contrast to EC-CO_2R GDEs, ODCs are typically carbon-free and instead entirely metal-based, such as a silver oxide catalyst supported on silver wire gauze substrate with hydrophobic PTFE used as binder.[45] Electrode scale-up was initially hindered by the hydrostatic pressure of the electrolyte, however this was eventually addressed through use of an elegant falling-film electrolyser (FFE) design.[44] This architecture uses a thin film of gravity-fed electrolyte that passes through a permeable material placed between the ODC and membrane. This 'percolator' acts as a flow resistor: as electrolyte moves through it under gravity, a pressure drop is generated that offsets the hydrostatic pressure build-up from the vertical column of liquid, thereby helping maintain a constant pressure at the electrode interface.

A 2022 review by Hernandez-Aldave & Andreoli examined the chlor-alkali ODC technology as a design platform for CO_2 GDEs.[43] It was proposed that similar design strategies – specifically the use of Cu-based GDEs and a FFE architecture – could be implemented in EC-CO_2R to address limited electrode lifespan and pressure imbalance. Technological crossover is non-trivial however as many chlor-alkali advancements remain proprietary and sparsely documented in published academic literature. Furthermore, EC-CO_2R introduces unique chemistry challenges, including CO_2 carbonation in alkaline electrolyte,[46] a diverse range of gaseous and liquid products,[47] and bubble formation within the catholyte.[48] Recently in 2023 Großeheide *et al.* described a 10 × 10 cm^2 reactor with 3D printed electrolyte flow frames.[49] This prototype was developed as a EC-CO_2R FFE however the underpinning principles of FFE operation were not explored: liquid and gas pressures were not measured, electrolyte percolation was qualitatively considered, and the electrode height (10 cm) was too short to reveal pressure imbalance effects relevant to scale-up.

Herein the fluid physics of percolation are elucidated, and the underpinning methodology for eliminating the hydrostatic pressure gradient is exploited for sub-millibar pressure control. By use of differential pressure monitoring, the delicate balance at the GDE interface is probed as a function of height. Thus, the first functioning FFE electrolyser for EC-CO_2R is reported here, and the consequences for achieving robust operation, that is essential for electrolyser scale-up, is explored.

2 Results and discussion

2.1 Theoretical interpretation of percolation

Fig. 1 shows a simplified diagram of a FFE in which electrolyte falls under gravity from a feed reservoir, passes through a porous percolator and into a lower drain reservoir. The electrochemical components are omitted here to focus on the fluid mechanical aspects. A pump recirculates the electrolyte to maintain a steady state with constant reservoir levels. Electrolyte moves in a continuous unbroken column such that the percolator is hydraulically connected to both reservoirs. The vertical elevations of the feed and drain reservoirs, and the top and base of the percolator, are denoted z_f, z_d, z_t and z_b respectively, relative to a vertical z-axis pointing upwards.

Fluids flow from regions of high to low mechanical energy: consisting of contributions from pressure, gravitational potential, and kinetic energy. In porous media flows, fluid velocities are typically low, so the kinetic energy term ($v^2/2g$) can be neglected. For incompressible flow, the mechanical energy per unit weight is expressed as the 'hydraulic head', given by the sum of the pressure and elevation heads at each vertical position z:

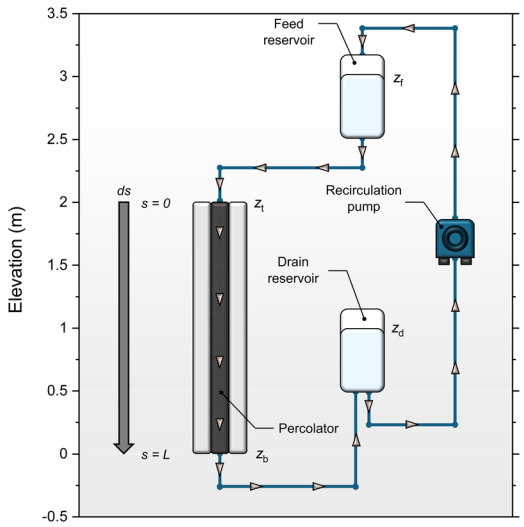

Fig. 1 Schematic of a simplified FFE system comprised of a percolator with feed/drain reservoirs. Elevation heads are given in terms of a vertical z-axis and the flow direction is indicated by grey triangular arrows.

$$h(z) = \frac{P(z)}{\rho g} + z$$

where ρ is the fluid density and g is the acceleration due to gravity. Noting here that all terms have units of meters and lateral coordinates (*i.e.* x and y) are irrelevant. In classical hydrology, flow through porous media is described by Darcy's law which relates the volumetric flux q to the gradient of hydraulic head along the direction of flow. Introducing a coordinate s that increases in the direction of fluid motion, Darcy's law takes the form:

$$q = -K\frac{\mathrm{d}h}{\mathrm{d}s}$$

where $K = \rho g k/\mu$ is the 'hydraulic conductivity', determined by the intrinsic permeability k of the porous medium and the dynamic viscosity μ of the fluid. In a vertical system where flow occurs downward and z increases upward, $\mathrm{d}s = -\mathrm{d}z$ and for steady flow through a homogeneous, isotropic porous medium, Darcy's law reduces to:

$$q = K\frac{\Delta h}{L}$$

where $\Delta h = h_t - h_b$ is the total head drop from top to base, and L is the percolator length which equals $z_t - z_b$ in the case of vertical alignment. In this formulation, $q > 0$ for downwards flow. In experiments, the measurable quantity is the total flow rate Q, which is related to the flux by the cross-sectional area A:

$$Q = A\frac{\rho g k}{\mu}\frac{\Delta h}{L}$$

Considering now how the hydraulic head is established at the top of the percolator, and assuming that head losses in the tubing and connectors can be neglected, then the pressure at the top of the percolator is set entirely by the hydrostatic pressure of the fluid column between the feed reservoir surface and the top of the percolator:

$$P_t = P_0 + \rho g(z_f - z_t)$$

Combining this with the expression for the hydraulic head at the top of the percolator:

$$h_t = \frac{P_t}{\rho g} + z_t = \frac{P_0 + \rho g(z_f - z_t)}{\rho g} + z_t = \frac{P_0}{\rho g} + z_f = h_f$$

shows that $h_t = h_f$, and a similar argument for the base of the percolator yields $h_b = h_d$. Therefore, the total head drop across the percolator is simply equal to the vertical distance between the feed and drain reservoir surfaces:

$$\Delta h = h_t - h_b = z_f - z_d = \Delta z_{Res}$$

This makes Δh a directly controllable parameter in experiments, adjustable by setting the relative heights of the reservoirs. Intuitively, increasing the elevation drop between the reservoirs increases the gravitational energy available to drive flow $q = K\Delta z_{Res}/L$, but the absolute elevations of the reservoirs do not affect the flow rate, provided their vertical separation remains fixed. That is, the reservoirs may be raised or lowered together without changing the flow rate.

Although the absolute elevations do not affect the flux, they do determine the internal pressure distribution within the percolator because of the magnitude of hydrostatic pressure applied to the percolator. Assuming uniform permeability and steady flow, the hydraulic head decreases linearly in the direction of flow. In terms of the vertical elevation coordinate z within the percolator ($z_b \le z \le z_t$), this can be written as:

$$h(z) = \left(\frac{P(z)}{\rho g} + z\right) = h_t - \frac{\Delta z_{Res}}{L}(z_t - z)$$

Therefore, the pressure function is:

$$P(z) = P_0 + \rho g\left[z_f - z - \frac{\Delta z_{Res}}{L}(z_t - z)\right]$$

Differentiating this with respect to z yields the vertical pressure gradient within the percolator:

$$\frac{dP}{dz} = \rho g\left(\frac{\Delta z_{Res}}{L} - 1\right)$$

This result highlights several important implications. Firstly, a vertical pressure gradient exists within the percolator in the general case, but this may be positive or negative depending on the ratio $\Delta z_{Res}/L$. If the reservoirs are placed at equal elevations ($\Delta z_{Res} = 0$), the result recovers the standard hydrostatic pressure gradient: $dP/dz = -\rho g$ whereby no electrolyte flows. If the elevation drop between the reservoirs is smaller than the length of the percolator ($\Delta z_{Res} < L$), the pressure still increases downward, though less steeply than in the hydrostatic case. Conversely, if the reservoir separation is greater than the percolator length ($\Delta z_{Res} > L$), then an upwards pressure gradient is encountered along the elevation z, *i.e.* the pressure is higher at the top of the percolator. These results are entirely physical, as fluids follow head gradients rather than pressure gradients. Solving the previous equation for $dP/dz = 0$ identifies a special case, whereby $\Delta z_{Res} = L$, corresponding to a critical configuration in which the pressure gradient within the percolator vanishes. In this case, the gain in hydrostatic pressure exactly balances the head loss due to flow resistance, resulting in a pressure that is constant with elevation. This uniform operating pressure is equal to the pressure exerted at the top of the percolator; likewise, this argument can be used to show that it is also equal to the pressure at the base, such that when $\Delta z_{Res} = L$, $P_t = P_b$. Under this condition, the system flows at a critical flow

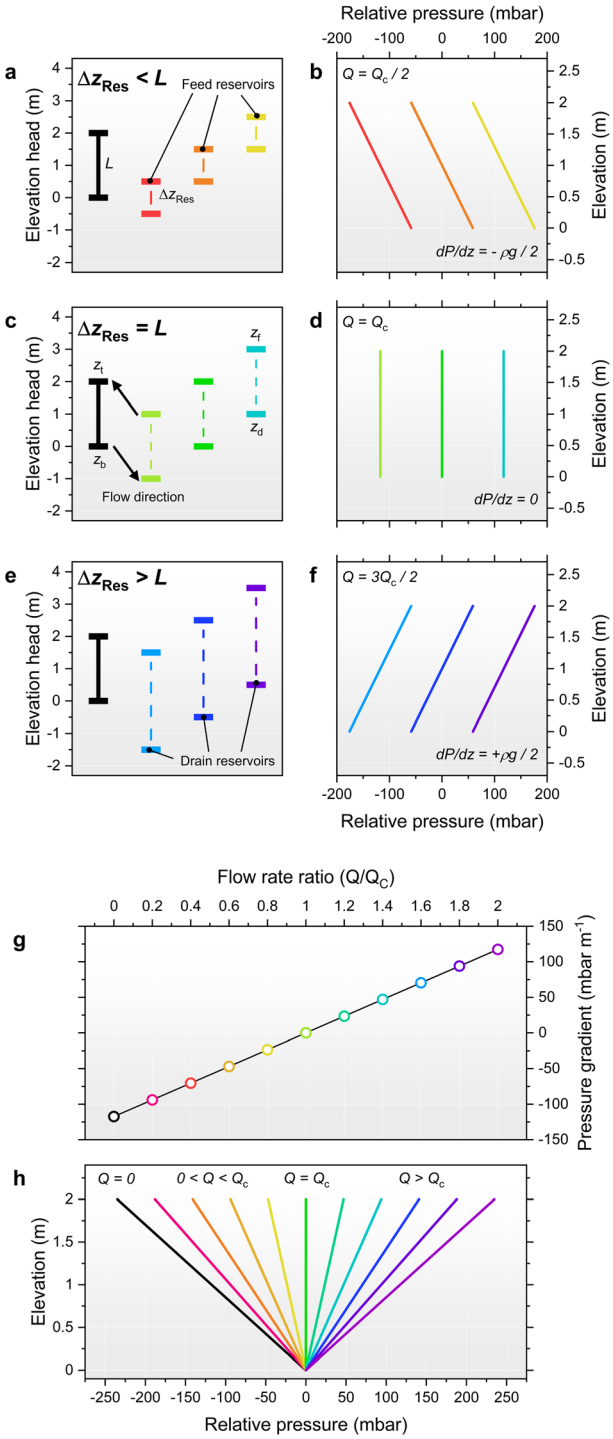

Fig. 2 Illustration of the effect of varying reservoir elevations relative to a percolator of 2 m height and fixed position, shown in black. In (a), (c) and (e), reservoir elevations are indicated by horizontal lines whereas elevation differences (Δz_{Res}) are indicated by dashed vertical lines. Corresponding pressure distributions within the percolator are shown in (b), (d) and (f) with $P_0 = 0$. The effect of varying Δz_{Res} from 1 to 2 to 3 m are shown in (a), (c) and (e) respectively, in addition to elevating or lowering both reservoirs by ±1 m. In (g) and (h) the relationship between flow rate (Q/Q_c) and the pressure gradient is shown in comparison to a static electrolyte (black). Pressures are displayed relative to the base of the percolator at $P_0 = 0$.

rate Q_c that depends only on fluid properties and percolator geometry:

$$Q_c = \frac{A\rho g k}{\mu}$$

Fig. 2 graphically illustrates the possible pressure distributions for a 2 m tall percolator using relative pressures, (*i.e.* $P_0 = 0$), and an electrolyte density of $\rho_{1M\ KHCO_3} = 1200\ kg\ m^{-3}$. The simplest case is shown in dark green in Fig. 2c whereby the reservoir elevations match those of the percolator top and base, resulting in a uniform pressure equal to P_0. The remaining curves in Fig. 2c represent moving both reservoirs up or down by 1 m, whilst keeping their elevation difference unchanged. This also results in a constant pressure but offset by $\pm\rho g \cdot 1$ m = ±117.4 mbar as shown in Fig. 2d. Flow rates for these constant pressure examples are all equal to the critical flow rate Q_c and are independent of the absolute elevations. In contrast, the examples in Fig. 2a and e yield decreasing or increasing pressure gradients because $\Delta z_{Res} \neq L$ (Fig. 2b and f, respectively). Again, the magnitude of pressure is also offset by a constant $\rho g \cdot 1$ m = ±117.4 mbar by shifting the reservoir pair by ±1 m. Given that values of Δz_{Res} were arbitrarily chosen here as 1 or 3 m, the pressure gradients are also arbitrarily $\pm\rho g/2$ = ±58.7 mbar m^{-1} with corresponding flow rates of $Q_c/2$ and $3Q_c/2$ for Fig. 2a and e, respectively.

More generally, the percolated flow rate is a continuous variable, thus, as an alternative viewpoint, the pressure within the percolator may be considered a function of the flow rate, $P(Q, z)$, as shown graphically in Fig. 2h for $P(0 \leq (Q/Q_c) \leq 2)$. Here the dimensionless flow ratio Q/Q_c serves as a useful parameter to characterise the flow (simply a re-expression of Darcy's law: $Q/Q_c = \Delta z_{Res}/L$) such that substitution yields:

$$P(z) = P_0 + \rho g\left[z_f - z - \frac{Q}{Q_c}(z_t - z)\right]$$

and pressure gradient:

$$\frac{dP}{dz} = \rho g\left(\frac{Q}{Q_c} - 1\right)$$

Intuitively, the pressure gradient increases from $dP/dz \geq -\rho g$ as the flow rate increases from static, because faster flow rates produce increasing hydrodynamic pressure drops at the top of the percolator.

2.2 Electrolyte flow, pressure and percolation

Electrolyte circulation through an electrochemical device enhances mass transport of reactants to electrode surfaces *via* convection whilst mitigating diffusion limitations. The circulation method is therefore important, yet the impact on GDE stability is overlooked in the literature given the use of unsuitable pumps. Before introducing a porous percolator, the effect of different circulation methods was measured to highlight the implications for GDE operation (Fig. S13). The use of peristaltic pumps in EC-CO_2R research is widespread,[33,34,50–53] however their design imparts flow pulsation as the flexible pump tubing is periodically compressed by the rollers. This causes extreme pressure fluctuations and significant noise during operation: a conventional 4-roller pump tested here gave an average pressure of 61 ± 56 mbar at 100 mL min^{-1}, however the full pressure range spanned from −34 to 140 mbar (Fig. S13a). Thus, this peristaltic pump would expose a GDL to a pressure range of more than 170 mbar, which is intolerable for most GDLs reported.[33] While it may be possible to mitigate the pulsation, such as by use of dampeners,[33] alternative pump designs are much more appropriate for application. For example, a gear pump tested under identical conditions gave an average pressure of 63 ± 3 mbar making it a more practical option for electrolyte circulation (Fig. S13d). Despite this, an undesirably large pressure range of 16 mbar was still measured which would be significant when operating conventional GDEs.

The use of pumps in laboratory research offers simplicity and convenience, however gravity-driven circulation is introduced here as an easy to implement and superior alternative. By using flow restricting valves placed below the electrolysis cell, the electrolyte flow rates and pressures can be conveniently controlled, whilst varying relative reservoir elevations as needed to set the magnitude of hydrostatic pressure applied to the cell. Such a configuration was constructed in this research for conventional EC-CO_2R experiments (Fig. S1 and S10). For comparison at 100 mL min^{-1}, this approach gave a very low noise (average of 9.8 ± 0.1 mbar, range of 0.5 mbar) and effectively constant electrolyte pressure (Fig. S13g). Considering now the pressure within the electrolyte as a function of elevation, a pressure gradient close to $-\rho g$, calc. −1.17 mbar cm^{-1}, was measured regardless of the circulation method used; pumped or gravity-driven (Fig. S13c, f and i). This was also comparable to the pressure gradient of a static electrolyte (Fig. S14). Therefore, in the absence of a percolator, the flow rate has little influence on the internal pressure gradient, and at a flow rate of 100 mL min^{-1}, the dynamic pressure contribution from flow is negligible compared to the gravitational component. In other words, without a porous medium to resist the flow, the system cannot achieve a uniform internal pressure profile.

Employing the simple apparatus shown in Fig. 3, the simplest configuration of a percolator paired with gravity-driven flow was first examined to identify suitable percolator materials and an electrolyte reservoir circuit that is effective for operation. To achieve this, a 'Hele-Shaw cell' (H-S), shown in Fig. 3a, was designed and constructed with a porous material compressed between two transparent acrylic plates for visual observation. It should be noted that while the term 'cell' is used in the porous-flow community,[54–56] this device is not intended for electrochemical operation. The cell does however

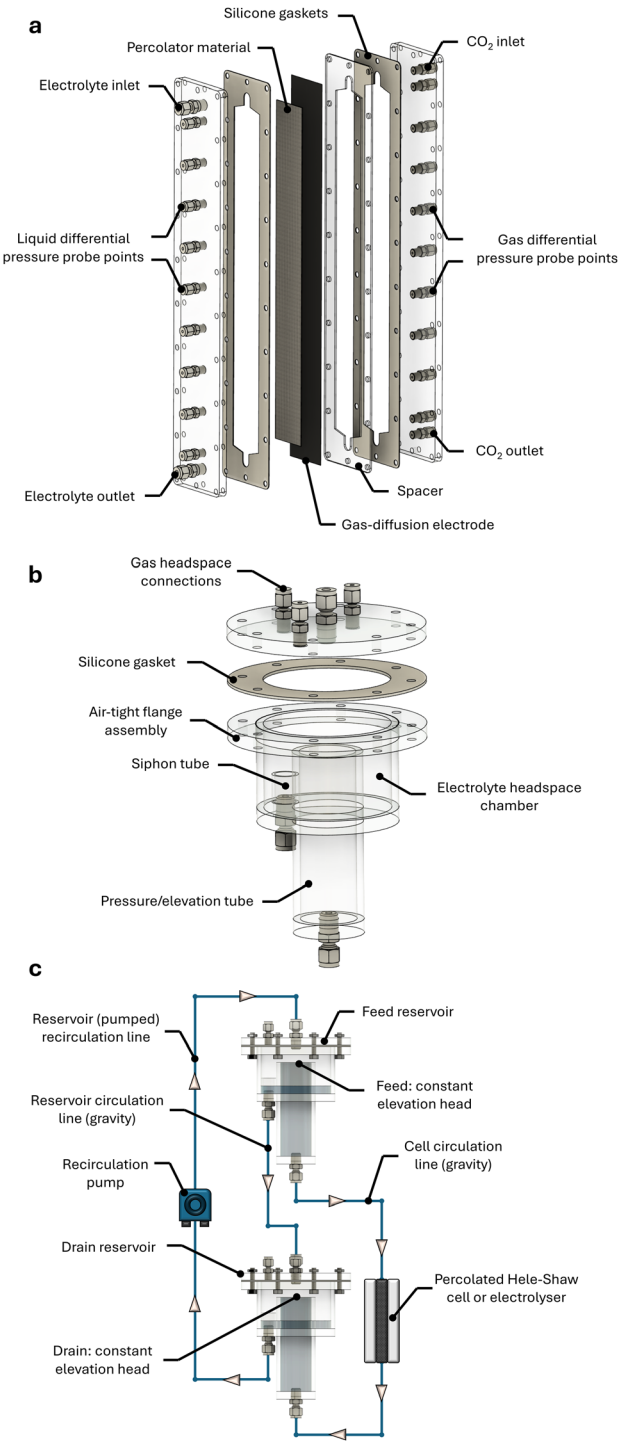

Fig. 3 (a) H-S cell featuring flowing electrolyte and CO_2 chambers, percolator, GDL and pressure sampling points; (b) geometry of the weir reservoirs employed for maintaining constant electrolyte elevation heads upon flow; (c) electrolyte circulation schematic showing the direction of falling liquid through a porous material.

incorporate probing points along its height for pressure measurement as was used in the above pressure measurements without a percolator. The H-S cell used in this work had a fixed 40 cm height by 5 cm width channel, with a variable thickness for testing different materials. This height was chosen because the corresponding hydrostatic pressure (~47 mbar) matches the lower end of the pressure stability range of commercial GDLs (~40 mbarD),[33] and because of the difficulty in procuring GDLs in lengths greater than 50 cm.

For the choice of percolator material, no commercial purpose-designed materials could be obtained. This is because percolators employed in commercial chlor-alkali electrolysers are proprietary, and little is disclosed besides a few materials mentioned in patents such as perfluorinated plastics,[57] high density polypropylene foam,[58] or woven/knitted fabrics.[59] It was hypothesised that any porous material could potentially serve as the percolator, however, materials that are readily wetted by the electrolyte and exhibit high porosity are likely to perform best. Wettability ensures uniform saturation and avoids dry patches, while high porosity improves fluid accessibility and mass transfer. Additionally, operation in an electrolyser necessitates high stability, mechanical strength, chemical resistance and electrical insulation due to direct cathode contact. Fortunately, many industrially manufactured plastics already meet these requirements and are negligibly expensive when compared to the other electrolyser components.

Based on system-design considerations, two different polymeric materials with contrasting porosity and structure were selected. Both are inexpensive polymers with excellent electrical insulation and chemical compatibility with 1 M $KHCO_3$ electrolyte that are ideal for scale-up. The structures of these materials are shown in optical microscope images in Fig. 4. The first is a fibrous sheet of 0.8 mm thickness composed of non-woven strands of polypropylene (PP). Despite being an inherently nonpolar polymer, the sheeting is easily wetted, and the material is commonly employed as a geotextile membrane for domestic drainage applications. While the individual fibres are consistently ~30 μm in diameter, the material is significantly inhomogeneous with a wide range of pore sizes varying from microns to millimetre. In contrast, the second material is a homogeneous open-cell

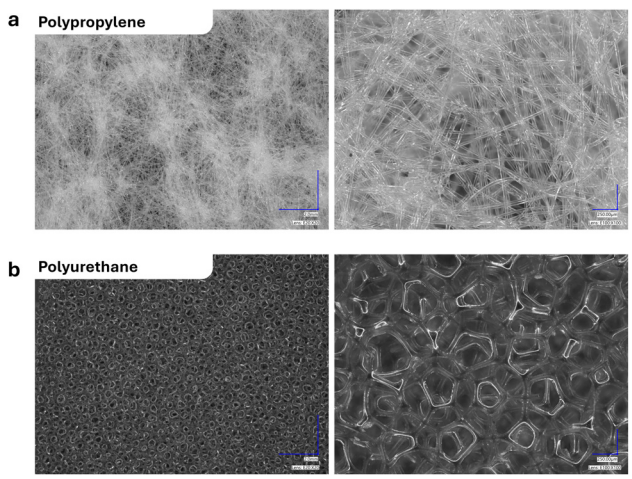

Fig. 4 Optical microscope images at ×20 and ×100 magnifications of (a) fibrous PP and (b) open-cell PU.

foam of 5 mm thickness and 80 PPI (pores per inch) that is composed of polyurethane (PU). Commonly used in packaging applications, the foam displays excellent mechanical and elastic properties resulting from the well-ordered structure and narrow pore size distribution. Indeed, measurements gave a typical pore diameter of ~200 μm with matrix thicknesses of ~60 to 70 μm.

Constructing a setup akin to Fig. 3, reservoir elevations of the feed and drain reservoirs were initially set to the elevations of the top and base of the percolator, respectively. To maintain constant electrolyte elevations during circulation, custom 'weir' reservoirs shown in Fig. 3b were designed and assembled into a flow circuit shown in Fig. 3c. The stability of flow from these reservoirs was monitored for 15 h, giving a negligible variation of ±0.7 mbar (Fig. S16a), demonstrating excellent control of pressure (±3.1 mbar variation over a 7-day period, Fig. S16b). Initially using the PP percolator, a pressure gradient of −0.25 mbar cm^{-1} was measured with a corresponding flow rate of 40 mL min^{-1}. Notably this gradient deviates from the idealised theoretical prediction, which neglects head losses from system constrictions. Consequently, head losses must be compensated by reservoir elevation adjustments accordingly. Simple analytical models such as the Darcy–Weisbach equation (see the SI),[60] for laminar flow in circular pipe, provide a useful approximation for the major losses (calc. ~2 cm per meter of tubing), but additional empirical adjustments were required to achieve the constant pressure distribution at zero pressure shown in Fig. 5b. A sub-millibar gradient of −0.07 mbar cm^{-1} was measured corresponding to merely 2.7 mbar variation across the 40 cm height of the percolator. Shifting both reservoirs by ±50 cm led to a corresponding shift in the gauge pressure by ±50 mbar, while the pressure distribution remained constant. The flow rate remained unchanged at 45 ± 1 mL min^{-1}, confirming that the throughput depends only on the reservoir spacing Δz_{Res}, and not on their absolute elevations. The same pressure compensation effect was obtained for the PU percolator, albeit with greater adjustments required due to more significant parasitic head losses at the higher ~200 mL min^{-1} critical flow rate resulting from the increased cross-sectional area tested (Fig. S17).

Comparison of the two materials highlights the importance of optimising flow rate because the constant pressure FFE operates at the critical flow rate Q_c, which is predominantly a function of percolator thickness and permeability. Many high power electrochemical devices adopt near zero-gap configurations for the benefit of optimising energy efficiency, however percolator thicknesses <1 mm would severely restrict the critical flow rate. Maximising percolator permeability is therefore important to ensure reliable flow. While permeability is predominantly a function of pore size and porosity, it is also dependent on practicalities such as compression, homogeneity, material layering, and assembly imperfections. Indeed, the flow rate given by Darcy's law is essentially a global average with differing flow pathways having varying flow rates within the material. For these reasons, an effective permeability k_{eff} should be considered when comparing materials. By orientating the percolator horizontally and measuring the pressure drop as a function of imposed flow rate, k_{eff} can be easily calculated. This configuration eliminates the elevation component of hydraulic head along the material ($\Delta z = 0$) simplifying Darcy's law to:

$$q = -\frac{k_{eff}}{\mu}\frac{dP}{dx}$$

where x is the coordinate from the inlet side of the material. Fig. 6 shows the measured pressure distributions $P(Q, x)$ and

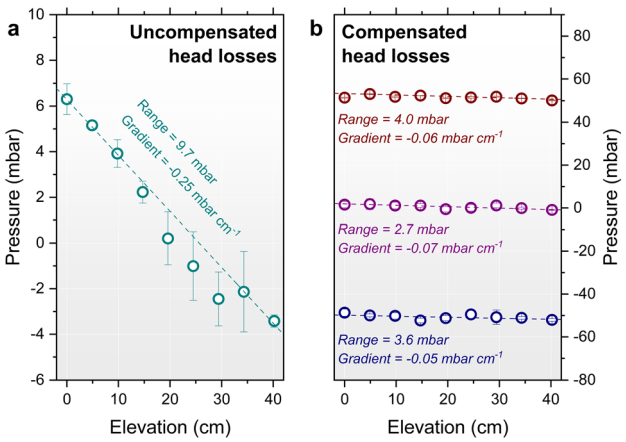

Fig. 5 Vertical pressure distributions along a 40 cm PP percolator: 2 layers compressed within a 1.5 mm gasket. The reservoirs were configured with $\Delta z_{Res} = L$ to give constant pressure distributions, however the effect of uncompensated head losses is shown in (a). With empirical compensation in (b), the pressure distributions are shown for configurations whereby the elevations of the reservoirs were adjusted by ±50 cm relative to the percolator. Elevation refers to both the vertical position along the percolator and the reservoir positions. Error bars show the standard deviations of average pressures of three repetitions.

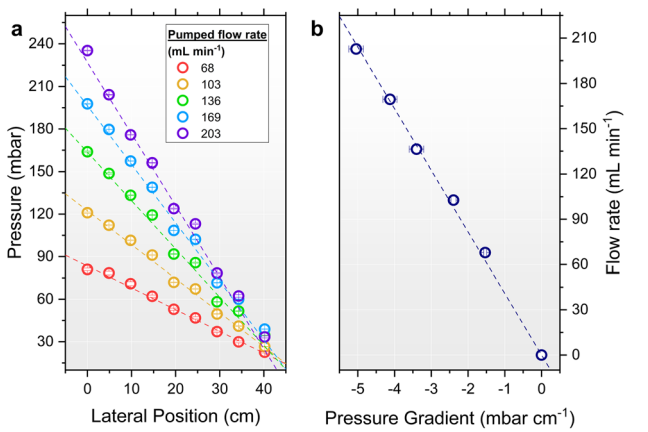

Fig. 6 (a) Determination of the k_{eff} of the PP percolator (2 layers compressed within a 1.5 mm gasket). The pressure drops resulting from variable imposed flow rate is shown with error bars representing the standard deviation of the average pressure recorded for 2 minutes; (b) corresponding pressure gradients are plotted *vs.* the applied flow rate. Linear regression was performed with the intercept set at the origin using the standard errors of the gradients in (a).

associated linear regression of $Q(dP/dx)$ which gave an k_{eff} of $(9.0 \pm 0.7) \times 10^{-10}$ m^2 for the PP material, whereas the same methodology applied to the PU foam yielded a higher k_{eff} of $(2.2 \pm 0.1) \times 10^{-9}$ m^2 (Fig. S18). These values place both materials within the range typically associated with well-sorted sands in hydrogeology,[61] though the difference in permeability is still significant as under identical conditions, the PU material provides over double the flow rate (calc. ratio = 2.4) with essentially no drawbacks. Reflecting on the insight gained from this study, it is valuable to revisit the work of Großeheide *et al.*, who reported a FFE electrolyser for EC-CO_2R.[49] Reiterating that a uniform percolated pressure distribution requires the electrolyte to flow at the specific Q_c of the system, it is not immediately evident that this was realised in their design. Indeed, neither the pressure distribution within their percolator or their system Q_c was measured. Specifically, their gravity-driven flow rate was not a passive consequence of reservoir elevations but rather controlled by fixed-rate pumping into an overflow reservoir feed design, however such a variable flow-rate approach would require the intentional quantitative measurement of Q_c to configure the system appropriately. We speculate that the Q_c for their system exceeded the 4 L min^{-1} flow rate utilised, which was chosen based on the apparent quality of flow distribution and percolator saturation. Thus, the hydrostatic pressure of the electrolyte was likely only partially compensated, *i.e.* a negative pressure gradient of $-\rho g \leq dP/dz < 0$. This commentary is intended to highlight the complexity of the fluid physics involved in deliberately achieving constant pressure FFE electrolysis conditions, and to underscore the importance of directly measuring and quantifying the critical flow characteristics.

2.3 Electrode differential pressure

The differential pressure (ΔP) across a GDE is defined as the difference between the liquid P_l and gas P_g pressures: $\Delta P = P_l - P_g$. In operating GDEs, ΔP is an important parameter to control because ΔP influences the position of the CO_2–electrolyte interface within the GDE, however it is very infrequently reported in the literature. Intuitively, a GDE is pressure 'balanced' when $\Delta P = 0$, however GDEs are also considered 'stable' when operated at non-zero differential pressure, suffice that no excessive CO_2 or electrolyte over-pressure is exerted on the GDE causing gas breakthrough (GBT) or electrolyte flooding (EF). Experimentally, the onset of GBT and EF can be defined by threshold pressures ΔP_{GBT} and ΔP_{EF} corresponding to the first appearance of gas bubbles or water droplets, respectively. GDEs are therefore stable when $\Delta P_{GBT} < \Delta P < \Delta P_{EF}$ and consequently, the magnitude of the pressure stability range (δP) of a GDE is given by $\delta P = \Delta P_{EF} - \Delta P_{GBT}$.

δP is a useful parameter to compare different GDE materials as vast variation has been reported depending on the thickness and porosity of the GDL/GDE. Baumgartner *et al.* evaluated various commercial GDLs and measured their threshold stability ranges.[33] δP varied significantly between 42 ± 14 and 464 ± 141 mbarD, however most materials gave a narrow stability range of $40 \lesssim \delta P \lesssim 80$ mbarD. These values represent best case scenarios, measured using pristine materials, as ΔP_{EF} is known to rapidly decrease during electrolysis due to electro-wetting.[42] Leonard *et al.* recorded that the ΔP_{EF} of Freudenberg H23C6 decreased significantly during operation, and the wetting rate was also a function of applied current density.[38] Normalised to 1000 mA h charge passed, the most severe degradation was at the highest current density tested (196 mA cm^{-2}, cathode potential of calc. ~−2 V *vs.* RHE), causing ΔP_{EF} to decrease from +642 to only +22 mbarD. This indicates that the stability range of GDEs is more restrictive in practice because operating at ΔP close to the thresholds ΔP_{EF} or ΔP_{GBT} likely accelerates electrode failure upon wetting.

GDEs are conventionally placed vertically to facilitate the upward removal of gas bubbles and avoid catalyst blockage. This orientation imparts an undesirable differential pressure gradient due to the difference in density between CO_2 and electrolyte. All fluids accumulate pressure as $dP/dz = -\rho g$, however the density of electrolyte is approximately three orders of magnitude higher than CO_2. Thus, the pressure of the CO_2 is effectively constant, whereas the electrolyte generates a gradient of roughly −1 mbar cm^{-1}. Consequently, the ΔP across a hypothetical 2 m height GDE would vary by ~200 mbarD, plausibly causing EF at the base and simultaneous GBT at the top, as illustrated in Fig. 7a where the CO_2 was balanced at half-height.

The GDL materials 'Sigracet 28BC' and 'Freudenberg H15C13' were selected for this work as being representative of GDLs frequently employed in EC-CO_2R research. The 28BC material has a total thickness of 235 μm and is composed of a non-woven paper CS with a 5 wt% PTFE MPL. The H15C13

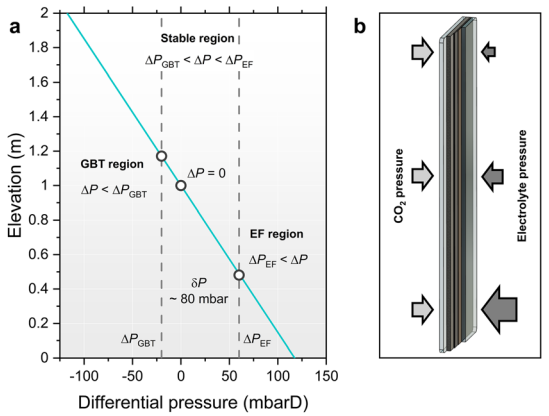

Fig. 7 (a) Graphical illustration of the interfacial differential pressure across a hypothetical 2 m tall GDE with 1 M $KHCO_3$ electrolyte, and pressure balanced CO_2 gas at mid-height. The hydrostatic pressure gradient in the electrolyte causes the differential pressure to increase with depth, dropping below the gas breakthrough threshold (ΔP_{GBT}) at the top and rising above the flooding threshold (ΔP_{EF}) at the base; (b) schematic of the GDE with arrows symbolising the magnitude of CO_2 and electrolyte pressures.

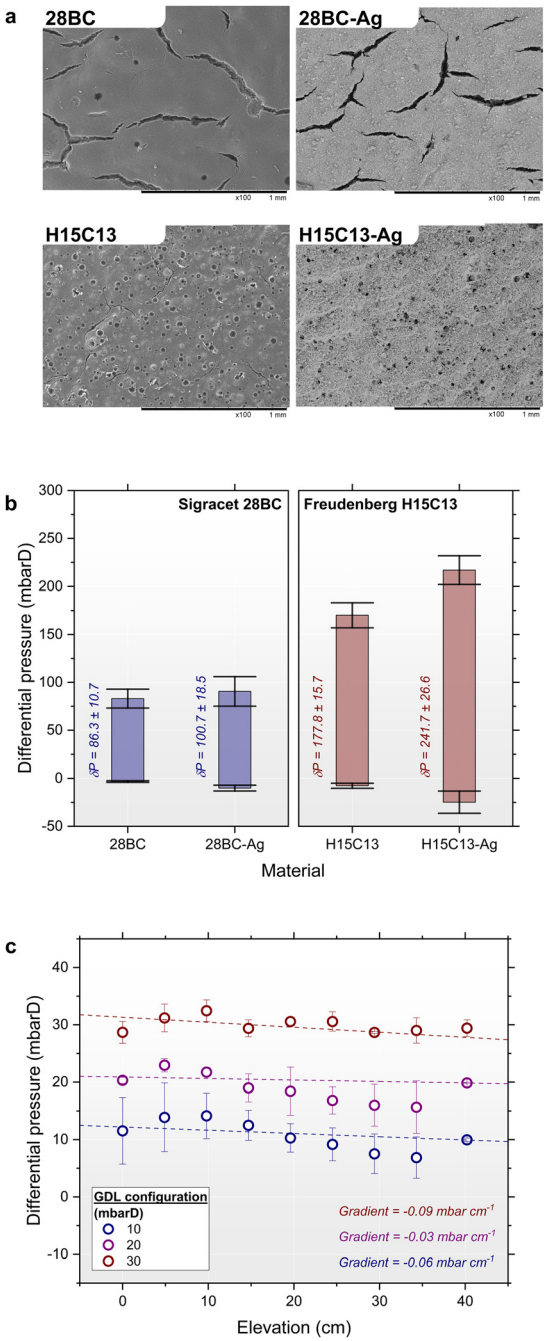

Fig. 8 (a) Scanning electron microscope (SEM) images at ×100 magnification of 28BC and H15C13 GDLs in comparison to spray-coated 28BC-Ag and H15C13-Ag GDEs; (b) differential pressure thresholds for GBT and EF (using 1 M $KHCO_3$) for the corresponding GDLs and Ag-GDEs in (a). Datapoints represent averaged results over three different GDE samples and error bars represent the associated standard deviations; (c) differential pressure as a function of height for a 28BC GDL with a PP percolator. Pressures within the H-S at different set CO_2 pressures are compared for the same reservoir elevations, resulting in ΔP values of +10, +20 and +30 mbarD. Elevation refers to both the vertical position along the percolator and the reservoir positions. Error bars represent the standard deviations of the average of three repetitions.

GDL has a similar construction but is thinner at 155 μm and the PTFE content is proprietary (assumed to be in the range of 0 to 10 wt%). The major difference between the materials lies in their surface condition. The 28BC GDL has a high surface coverage of cracks that penetrate deep into the MPL, with an approximate width of 50 μm (Fig. 8a). In commercial fuel cells these cracks are intended for improved water management within the electrode assembly.[34,62,63] However in a CO_2R electrolyser where EF must be avoided, these cracks function as defects whereby EF or GBT occurs at lower breakthrough pressures compared to the pristine MPL areas.[33,64] In contrast to 28BC, the H15C13 GDL is essentially defect-free making it far more pressure resilient. This was quantified by measuring ΔP_{EF} and ΔP_{GBT} at the GDL interface under flow-by pumped conditions using a modified electrolysis cell and a differential pressure meter (Fig. S11a).

Fig. 8b shows the pressure stability regions for the 28BC and H15C13 GDLs in comparison to corresponding GDEs with spray-coated catalyst layers (28BC-Ag and H15C13-Ag). Silver nanoparticles and Nafion® resin was used for the catalyst ink formulation in this work due to the simple catalysis of CO_2 to CO which is robust and reproducible. In addition, the competing hydrogen evolution reaction (HER), which is known to dominate the catalysis upon electrode wetting, is a useful metric to quantify GDE degradation and performance loss. For the 28BC GDL, the thresholds for GBT and EF were ΔP_{GBT} = −3.2 ± 0.9 mbarD and ΔP_{EF} = +83.0 ± 9.8 mbarD, respectively. In context of published results,[33] 28BC (235 μm) is assumed to be similar to the familial 22BB (215 μm) and 39 BC (325 μm) GDLs albeit with nominal thickness difference, yet the 28BC exhibited higher resistance to flooding by approximately ≅39 and ≅16 mbar, respectively, in our measurements. In addition, while it was assumed that ΔP_{GBT} for GDLs is 0 mbar in the literature,[33] a non-zero threshold was measured here (−3 ± 0.9 mbarD) which indicates that the GDL can tolerate mild CO_2 over-pressure operation. In contrast, the H15C13 GDL showed greater pressure resilience with ΔP_{GBT} = −7.7 ± 2.6 mbarD and ΔP_{EF} = +170.0 ± 13.1 mbarD, however flooding resistance was significantly less than reported results of the thicker 250 μm H23C6 GDL with ΔP_{EF} = +464 ± 141 mbarD in ref. 33 and +642 ± ~150 mbarD in ref. 38. As shown in Fig. 8b, the GDLs demonstrate reasonably large pressure stability windows of δP = 86.3 ± 10.7 mbarD and 177.8 ± 15.7 mbarD for 28BC and H15C13, respectively. These values increased further upon catalyst loading, whereby the thresholds for both GBT and EF were both advantageously improved, increasing δP to 100.7 ± 18.5 mbarD and 241.7 ± 26.6 mbarD for 28BC-Ag and H15C13-Ag GDEs, respectively. This observation contrasts with published trends, where GDEs were typically reported to be less resilient to EF, possibly due to differences in catalyst layer composition.[38] Regardless, these measurements suggest that electrodes of 1 or 2 m height could in theory tolerate the associated hydrostatic column pressure, however these measurements reflect the pristine material and neglect deterioration *via* wetting. In addition, repeated pressure measurements performed here highlighted the significant variability between electrodes tested, with notably large deviations of ΔP_{EF} thresholds. In contrast, measurements of

ΔP_{GBT} were consistently less variable which indicates that the propensity for EF varies more between different samples and production batches of the material. This observation can be rationalised by considering that these threshold pressures correspond to capillary pressures (P_c) associated with the GDL pore structure.

Assuming a cylindrical pore geometry, the capillary pressure can be approximated by a simplified Young–Laplace relation:

$$P_c = P_l - P_g = -\frac{2\gamma \cos\theta}{r}$$

where γ is the interfacial liquid–gas surface tension, θ is the contact angle measured through the liquid phase, and r is the effective pore radius.[65] In a hydrophobic GDL ($\theta > 90°$ and $\cos(\theta) < 0$), this relation predicts that electrolyte flooding requires a positive liquid overpressure to overcome the capillary entry barrier. High hydrophobicity (large θ) and small pore radii in the MPL both increase the flooding threshold. However, defects such as cracks in the MPL create orders of magnitude larger pore radii than the nominal average, lowering the local flooding threshold. Because flooding is initiated at the weakest point, ΔP_{EF} is effectively determined by the largest defect present. In the case of GBT, CO_2 displaces electrolyte (with the contact angle still defined by the electrolyte so that $\theta < 90°$ and $\cos(\theta) > 0$), giving negative values for the capillary invasion pressure. The magnitude of ΔP_{GBT} is also expected to be small as the bulk electrolyte lacks porosity, (effectively a very large pore radii) and thus the variability correspondingly less significant than that of ΔP_{EF} caused by MPL defects.

The effect of limited GDE pressure stability is evident even for GDEs only 45 cm tall. Introducing now a 28BC GDL into the H-S cell fitted with a secondary chamber containing CO_2 flow, the practicalities of vertically scaled GDEs were examined. This arrangement enabled direct observation of the GDL CO_2–electrolyte interface under variable differential pressure as a function of height. Firstly, when using a low-noise gear pump to circulate electrolyte upwards past the GDL (without a percolator), the hydrostatic column pressure means that the differential pressure may only be balanced at one vertical point (by varying the CO_2 pressure) giving $\Delta P < 0$ above and $\Delta P > 0$ below that point. When balancing the differential pressure at the top of the GDL, it was possible to operate the entire GDL without any EF or GBT occurring, because the differential pressure at the base of the electrode was +38.7 mbarD and therefore less than ΔP_{EF} (Fig. S19). In contrast, the electrode was not stable when attempting to balance the GDL differential pressure at mid-height or lower because of excessive GBT occurring at the top. Indeed, it was not possible to balance the differential pressure at 32 cm height or lower because any increase of the CO_2 back-pressure on the cell only accelerated the rate of GBT, rather than increasing the CO_2 gauge pressure. A similar phenomenon was observed when attempting to balance the GDL at mid-height and the differential pressure oscillated (Fig. S20a). This was an artefact caused by periodic GBT at the top of the GDL, such that as the CO_2 pressure increased, ΔP_{GBT} was eventually surpassed causing a wave of CO_2 to breach the GDL until the CO_2 pressure decreased and $\Delta P > \Delta P_{GBT}$ once more.

Switching to gravity driven and percolated flow proved initially challenging due to difficulties with filling the two-compartment H-S cell with electrolyte, especially when flow rates were slow, due to the polymeric materials being somewhat resistant to wetting and prone to withholding air bubbles. Additionally, problems arose from the flexibility of the 5 cm width GDL, such that the electrolyte pressure caused the GDL to deform and create voids around the percolator. This created pathways for faster flow and partial hydrostatic pressure gradients. These issues were resolved by pre-saturating the percolator before assembly and by introducing a supporting rigid metal mesh layer positioned behind the GDL to mitigate deformation; akin to the 'elastic elements' employed in commercial chlor-alkali electrolysers.[43] Regardless, the elimination of hydrostatic pressure was achieved in this configuration as shown in Fig. 8c. By adjusting the CO_2 pressure, the ability to manipulate the interfacial differential pressure from +10 to +30 mbarD was also demonstrated, which confirms that the electrolyte and CO_2 pressures are independently controllable. Given that the ΔP_{GBT} is very small for the 28BC GDL, operating the cell at $\Delta P \approx 0$ mbarD proved unreliable because the GDL was prone to GBT which adversely disturbed the measurements. In addition, relatively large repetition errors were measured because of the stop-start nature of moving the pressure sensor between sampling points, and the variability in the percolated flow. Despite this, sub-millibar differential pressure gradients were obtained from the averaged data (largest at −0.09 mbar cm^{-1}) and within experimental error. Interestingly, a wave-like variability in the measurements was observed which was attributed to uneven compression of the percolator, and possibly also the inhomogeneity of the PP permeability.

2.4 Falling film electrolyser

Operating an electrochemical flow cell with a percolator adds complexity due to the additional electrochemical cell components. The electrolysis process necessitates a counter reaction at the anode that is fed by an independent anolyte separated from the catholyte by an ion exchange membrane. Designing the membrane assembly was challenging because polymeric membranes are flexible and tend to swell in contact with electrolyte, which makes the percolator compression inadequate to ensure percolated flow. To mitigate this issue, a narrow flow cell with a geometric electrode area of 32 × 1 cm^2 was designed as shown schematically in Fig. 9a. The electrode width was kept small to minimise GDE and membrane deformation; however, the design was also constrained by the potentiostat current limit,

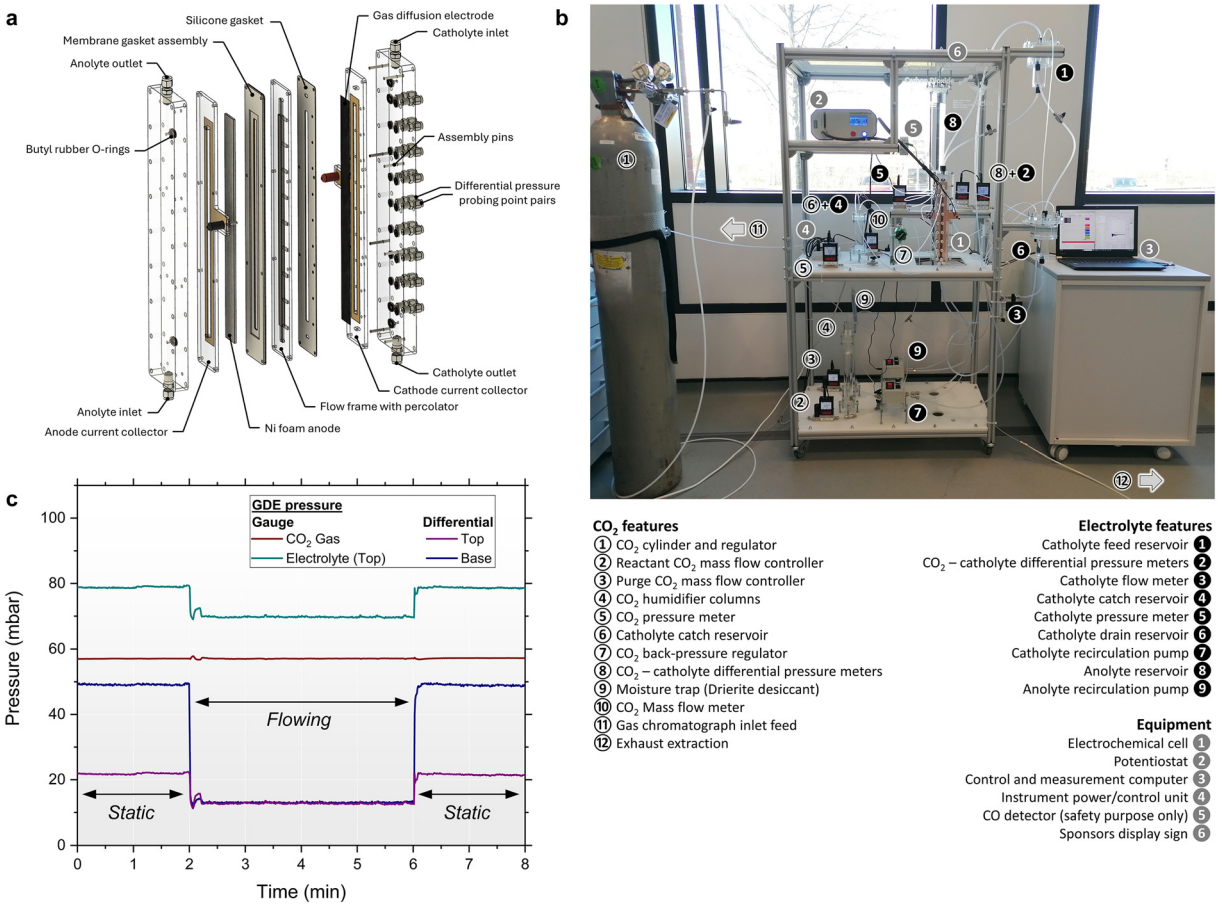

Fig. 9 (a) Illustrative diagram of the 32 × 1 cm^2 FFE cell featuring a percolated CO_2 GDE and differential pressure sampling points; (b) photograph of the gravity-fed FFE platform with all features annotated; (c) pressures monitored across the GDE height within the FFE with and without gravity-driven flow using a PU percolator. Electrolyte was flowed under gravity between 2 and 6 min to fully eliminate the catholyte hydrostatic pressure.

which restricted the feasible total electrode area. To further ensure percolator compression, a rigid nickel foam anode was employed in direct contact with the membrane, creating a zero-gap configuration. With adequate compression of the electrode assembly, it was not necessary to flow the sacrificial anolyte under gravity or through a pressure-controlling percolator. Anolyte was instead pumped upwards at a fixed 100 mL min^{-1} flow rate using a low-noise gear pump. The hydrostatic column within the anolyte had no measurable impact on the percolated GDE pressure distribution during operation of the FFE.

For the percolator assembly, a custom designed flow frame was 3D printed to house each percolator material and provide channels for electrolyte pressure measurement (Fig. 9a). Resulting percolator thicknesses were approximately 3 or 5 mm due to additional gasket layers and 3D printing limitations. While the percolator thickness was comparable to the H-S cell, the reduced width resulted in lower measured critical flow rates. For the PU foam material exhibiting a higher k_{eff} and thicker cross-section, a consistent Q_c of 165 mL min^{-1} was measured. In contrast, the thinner PP material gave a very low Q_c of ≤10 mL min^{-1} which was prone to blockage and too unreliable for use in the thin prototype FFE.

We hypothesise that the thinner PP percolator would provide sufficient electrolyte convection for the EC-CO_2R process because reaction rates are typically CO_2 mass transport limited. This remains to be examined in future work employing a scaled-up FFE prototype whereby the higher Q_c (proportional to percolator width) would likely result in reliable circulation.

The percolator thickness also directly impacts ohmic losses by increasing interelectrode separation. To quantify the magnitude of cell resistance under different assembly configurations, EIS (electrochemical impedance spectroscopy) was used to measure the ohmic resistance (Fig. S31b). The minimum cell resistance, corresponding to an interelectrode separation of ~3 mm and no percolator, was measured at 292 mΩ, equivalent to a cell resistivity of ~31 Ω cm. The addition of the PP percolator increased the cell resistance to 409 mΩ (44 Ω cm), whereas in comparison, the additional catholyte width at ~5 mm gave 576 mΩ (37 Ω cm) and the use of PU percolator increased the resistance further to 677 mΩ (43 Ω cm). Equivalent cell resistivities were calculated for the two percolators, thus indicating similar ion conductivity within their pore structure. Despite this, their use constitutes a noteworthy additional ~100 mΩ cell resistance compared

to the percolator-absent controls. At high current densities these ohmic losses constitute undesirable energy efficiency losses, making the percolator thickness, and associated flow rate-resistance trade-off important to optimise.

During FFE operation, a constant vertical differential pressure profile was first established by adjusting the reservoir elevations as before. The pressure distribution was monitored and measured by use of two independent differential pressure meters that probed the GDE interface at the top and base of the FFE. Thus, the overall pressure gradient ($dP/dz = (P_t - P_b)/L$) between the top and base is used here as a suitable measurement of vertical differential pressure. In establishing the percolated flow for electrolysis, the FFE principle was first demonstrated by measuring the pressure distribution sequentially under static and flowing conditions. This method is shown in Fig. 9c, whereby a valve placed between the FFE and drain reservoir was initially closed between 0 and 2 min, then opened for a 4 min duration to enable gravity-driven flow, and finally closed once again at 6 min. This highlights how the hydrostatic gradient was immediately and fully eliminated by the precisely calibrated FFE configuration upon gravity-driven flow at Q_c. The stability of the GDE pressure was measured for at least 8 h in a control experiment (Fig. S21) and was found to be typically stable within $-0.1 \leq dP/dz \leq +0.1$ mbarD cm^{-1}. Despite this, some pressure drifting was observed in electrolysis experiments due to apparent changes in percolated flow rate, thus affecting head loss compensations and the pressure distribution. This issue was noteworthy for the small-scale prototype employed here, because reservoir elevations and CO_2 back-pressure were set at the start of experiments and not adjusted thereafter.

Fig. 10 shows an 8 h EC-CO_2R experiment employing a H15C13-Ag GDE and PU percolator at a galvanostatic current density of 10 mA cm^{-2}. By adjusting the CO_2 back-pressure, the entire GDE interface was preconfigured at a target differential pressure of 0.0 ± 1.0 mbarD. This was chosen to demonstrate perfect pressure balance and to eliminate the pressure component of wetting. Owing to the low ΔP_{GBT}, resulting from the combination of the MPL and CL, no GBT was observed at this applied differential pressure. Fig. 10d show the pressure stability over the 8 h period whereby the GDE differential pressure gradient was on average +0.03 ± 0.05 mbar cm^{-1} (equivalent to an average pressure difference between the top and base in the sub-millibar range of +0.92 ± 1.67 mbarD), thus demonstrating the effective elimination of hydrostatic pressure from a time-averaged perspective. Despite this, when monitoring the electrolyser pressures on a second-by-second timescale, the magnitudes of differential pressure were frequently noisy with typically 4 mbarD of variation. This arose from the electrochemical reactions, such as the evolution of product gas bubbles from the CL which likely cause additional head losses, thus affecting the precisely calibrated hydraulic heads. An additional ΔP step change at 5.6 h was observed which originated from the corresponding CO_2 gas pressure step. This was attributed to

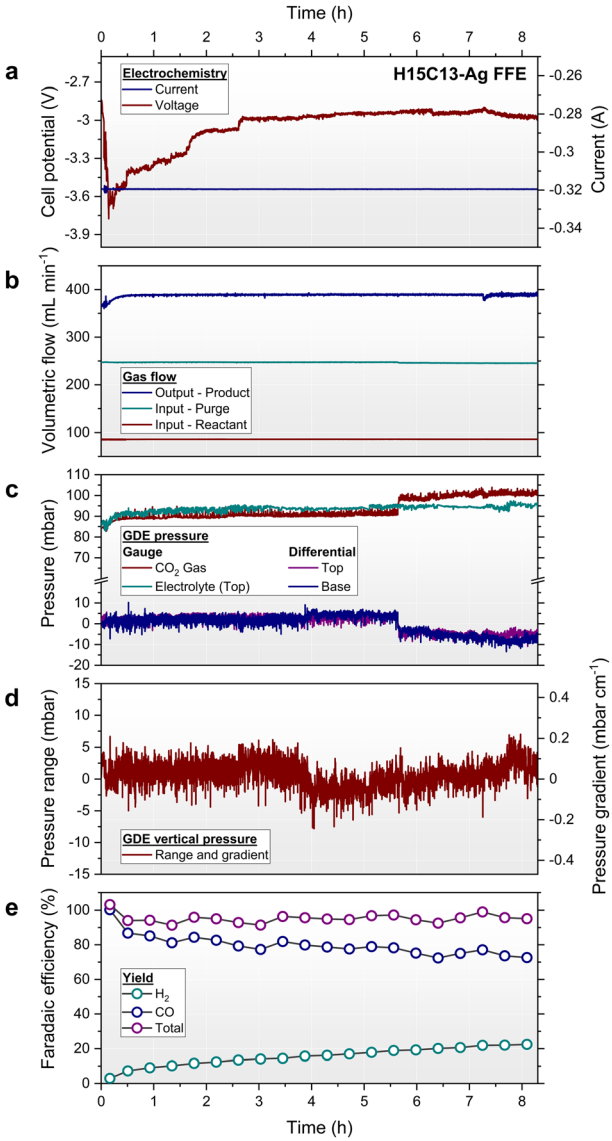

Fig. 10 EC-CO_2R at a H15C13-Ag GDE with constant vertical pressure and a percolated gravity-driven catholyte, using a PU foam percolator, at 10 mA cm^{-2}. The (a) cell potential relative to the working electrode, (b) CO_2 flow rates, (c) GDE pressures, (d) vertical GDE pressure range and gradient, and (e) faradaic yields are presented.

an artefact of the analogue back-pressure CO_2 regulator caused by its limited pressure control accuracy at the millibar scale.

Concurrently to the GDE pressures, Fig. 10a shows the corresponding electrochemical response. Despite the low 10 mA cm^{-2} current density applied, an initially high cell voltage in excess of 3.6 V was recorded, which was then followed by a relatively stable voltage of 3 V after 2.5 h. Given that the thermodynamic cell voltage for CO production coupled with the oxygen evolution reaction (OER) is calc. 1.33 V, high overpotentials were apparent which are not explained by ohmic losses (calc. 217 mV) alone. Corrosion of the nickel anode was observed during electrolysis which indicated significant OER overpotential, however the EC-CO_2R reaction

is also known to be kinetically limited and likely contributed to the high cell voltage. Additionally, product gas nucleation and evolution at the catalyst surface decreases the effective electrochemical area, making galvanostatic experiments susceptible to higher cell voltages. In an idealised system, gaseous products would diffuse back through the GDE and into the CO_2 gas stream, however despite the near-zero GDE differential pressure, bubbles within the catholyte flow were observed. In a conventional pumped electrolyser, buoyancy would be exploited to rapidly remove gas bubbles by pumping electrolyte upwards, however here the flow is downwards, making gas bubble management an issue for the FFE design. In operating this prototype electrolyser, a steady rate of bubbles emerging from the cell outlet and flowing downwards was observed, however it was uncertain how many gas bubbles remained suspended within the percolator. This observation likely explains why the maximum operating current density was limited to ~50 mA cm^{-2} at which cell voltages exceeded the 5 V potentiostat limit. This explanation is further supported by attempts made to increase the current density *via* increasing the catalyst loading to 2 mg cm^{-2}, or by increasing the CO_2 reactant flow rate to 300 mL min^{-1}, which made negligible performance improvements. The Ag-GDEs were imaged after electrolysis experiments *via* SEM in this study, but no apparent changes of the Ag catalyst layer were identified, excluding electrolyte precipitation, as reported by others in the literature (Fig. S26 and S28).[22,66,67]

The silver nanoparticles employed herein predominantly catalyse the production of CO, but parasitic H_2 is also generated at high cathode potentials. Fig. 10e shows the catalyst faradaic efficiency as a function of time, whereby the initially 100% CO yield decreased to 73% after 8 h. Concurrently, the H_2 yield increased linearly from 3% to 22%, with the total yield of products being quantitative (95.3 ± 2.6% on average). Given that the H_2 yield was initially very low, the increasing H_2 production rate is attributed to electro-wetted carbon within the GDE structure driving HER.[22,53,68] This is corroborated by the decrease in cell voltage to 3 V in Fig. 10a, which suggests an increase in electrochemical surface area, and associated lower cathode current density, rather than HER driven by overpotential. Indeed, in all FFE EC-CO_2R experiments performed herein, the GDEs were typically flooded by electrolyte in under 10 min of operation, with slow electrolyte permeation through the GDE occurring *via* droplets forming on the reverse side of the GDE. In the Fig. 10 experiment, a total of 38 mL of electrolyte was collected in the catch vessel over 8 h, corresponding to a flooding rate of approximately 5 mL h^{-1}. GDE flooding is a well-known stability problem for CO_2R at carbon-based electrodes due to hydrophobicity loss of the MPL,[36,69,70] however its impact here was significant for the FFE prototype tested. Using flooding rates and CO faradaic efficiency retention as metrics for electro-wetting, GDE stability was quite variable in this study. GDE flooding was measured within a range of ~1 to 10 mL h^{-1}, whereas CO efficiency retention after 8 h varied between 22 and 93%. While the H15C13-Ag GDEs tested gave reproducible results (Fig. S36 and S37 at 10 and 20 mA cm^{-2} respectively), the 28BC-Ag GDEs gave inconsistent stability and performance. Instability of 28BC-Ag was attributed to the surface cracking of the 28BC GDL making the material more susceptible to flooding. With surface defects observed to significantly vary between samples and production batches of the material, it proved challenging to reproduce 28BC-Ag experiments and make robust comparisons to H15C13-Ag. For electrolysers employing large GDEs, the quality of the electrolyte barrier becomes more critical because electrolyte flooding predominantly occurs at the worst defects in the material where electrolyte bypasses the MPL and easily penetrates the CS. Upon testing 28BC-Ag GDEs, the GDEs were stable for 8 h in some instances, giving similar response to H15C13-Ag in terms of differential pressure, cell voltage and flooding rate. The effect of electro-wetting was still prevalent however, with typically faster decay rates of CO faradaic yield observed (see the SI). In other instances, some 28BC-Ag GDEs completely failed within 2 h of operation (Fig. S34 and S35) due to a blockage of catholyte flow to the GDE. In these cases, the electrolyte flooding rate through the GDE was much faster and consequently, the reactant CO_2 flow behind the GDE was frequently blocked by electrolyte, causing the observed pressure spikes in experiments (see the SI). In the most severe cases CO_2 flow was fully obstructed causing GBT at the top of the GDE and escape of CO_2 upwards *via* the catholyte feed reservoir, in turn halting electrolyte flow. This unexpected mode of electrolyser failure was likely a consequence of the small prototype design; however, it highlights the difficulty in operating a passively flowing design.

Operating an EC-CO_2R electrolyser with a vertically constant GDE differential pressure profile is intended to eliminate the effect of pressure-wetting at the base of the GDE. Thus, the contribution of hydrostatic pressure on GDE stability was examined by comparison with control experiments utilising a conventional pumped catholyte. In these experiments the electrolyser lacked a percolator, and the electrolyte was pumped upwards at 165 mL min^{-1}, which is equivalent to the critical flow rate in prior FFE experiments. This circulation method resulted in a hydrostatic pressure column as expected, with a characteristic average gradient of ~−1.1 mbar cm^{-1}. To avoid GBT occurring during electrolysis, the GDE was balanced at the top giving a difference of ~+35 mbarD at the base of the electrolyser. In comparison to FFE experiments, the pumped experiments for 28BC-Ag and H15C13-Ag gave comparable results (Fig. S38 and S39). Indeed, the control experiments were still limited to low current densities (<50 mA cm^{-2}) with cell voltages exceeding 3 V. This suggests performance limitations of the electrode and catalyst assembly used[71] or the difficulty in operating large GDE areas, rather than any specific disadvantage of the FFE architecture, because these control experiments are directly analogous to literature studies.[66,67,72–77] For example, Ma *et al.* reported partial current densities for CO production at air-brushed Ag

nanoparticles on Sigracet 35BC GDLs exceeding 200 mA cm^{-2}.[76,77] Whereas Dinh *et al.* demonstrated extended 100 h testing at >150 mA cm^{-2} of Ag nanoparticle sputter-coated PTFE-based GDEs for flooding mitigation.[73] In both examples the electrode assemblies were highly optimised for high current density operation, but only using 1 cm^2 GDE areas and reference electrodes to control the cathode potential.

In this study, regardless of the electrolyte circulation method used, all GDEs typically became electro-wetted within 10 min of operation and flooded at similar rates thereafter. Water contact angle measurements performed on the post-electrolysis Ag-GDEs showed near identical angles (~90° within uncertainty) for FFE and pumped control experiments (Fig. S29). This indicated significant hydrophobicity loss compared to their initial pristine state (angles of ~140 and ~150° for 28BC-Ag and H15C13-Ag, respectively) and likely the complete wetting of the electrolysed GDEs.[34] Considering the similar performance between the FFE and pumped-electrolyte experiments, the benefit of sub-millibar differential pressure gradients at the GDE interface was severely undermined by electro-wetting, which is far more significant than the ~35 mbar pressure gradient generated within the prototype electrolyser tested here. We anticipate that GDEs demonstrated at pilot-scale with at least ~1 m height, and with improved resilience to electro-wetting, are required to demonstrate the enhanced GDE stability resulting from the elimination of hydrostatic pressure in vertically scaled electrolysers. Mitigating the electro-wetting of carbon-based GDEs remains a critical challenge for the EC-CO_2R research field,[78] as implementation of the technology necessitates electrode lifetimes of years.[10] Various approaches for managing GDE wettability have been explored to date such as mitigating electrolyte salt precipitation *via* periodic flushing with pure water[79] or electrode regeneration,[80] oleophobic GDE treatments,[65] preventing the adsorption and/or production of hydrophilic oligomers on the electrode,[41] or development of carbon-free GDEs akin to the ODC technology.[40,73] Yet the absence of bespoke commercial GDEs with flooding resistance for EC-CO_2R remains a problematic barrier for technological development.

3 Conclusions

For the first time, a gravity-driven percolated CO_2 electrolyser achieving vertically constant gas diffusion electrode differential pressure is fully demonstrated. Functioning as a flow resistor, the percolator counteracts electrolyte hydrostatic pressure and, given the correct configuration of reservoirs, produces constant pressure as a function of height. By use of Darcy's law, the fluid dynamics of operation were rationalised and the design aspects of a FFE EC-CO_2R electrolyser were presented:

(1) The vertical elevation difference Δz_{Res} between the feed and drain reservoirs is the most critical parameter to control and should (in the absence of parasitic losses) be configured such that $\Delta z_{Res} = L$, where L is the percolator vertical height, resulting in a zero pressure gradient $dP/dz = 0$.

(2) In real systems, reservoir elevations require additional empirical adjustments to compensate for parasitic head losses. Measuring the differential pressure at the top and base of the electrode is required to manage these losses.

(3) $\Delta z_{Res}/L$ determines the pressure gradient, however the magnitude of the constant pressure is dependent on the elevation of the reservoirs relative to the electrolyser. Thus, the pressure should be deliberately manipulated by raising or lowering both reservoirs by the same height adjustment as needed.

(4) When $dP/dz = 0$, the electrolyte flows at the critical flow rate Q_c which is entirely dependent on physical constants and percolator dimensions, allowing indirect control of the gravity-driven flow rate.

(5) Optimising the percolator thickness is important because of the trade-off between flow rate and cell resistance. In general, the thickness should be minimised to improve electrolyser energy efficiency.

(6) The percolator composition and porosity determine its permeability (k_{eff}). This parameter is an important property to optimise for enhancing flow rate, electrolyser mass transport, and gas bubble management.

Using this approach, a prototype FFE was demonstrated for EC-CO_2R with a Ag catalyst for CO production as a proof-of-concept. In 8 h electrolysis experiments at ~10 mA cm^{-2} current density, negligible pressure gradients of approximately ±0.1 mbar cm^{-1} were maintained across 32 cm tall GDEs. Under these conditions, the prototype performed similar to control experiments with a conventional pumped electrolyte due to the detrimental effects of electro-wetting. Thus, the benefits of constant GDE differential pressure are anticipated to become apparent when tested at pilot-scale utilising wider (>1 cm), taller (>32 cm) and more stable GDEs (>8 h). Consequently, significant electrode advancements are needed to mitigate the limited electrode lifetimes of carbon-based GDEs to avoid surface defects and hydrophobicity loss. Further development and optimisation of the FFE architecture and electrode assembly for EC-CO_2R are required to demonstrate industrially relevant current densities building on the prototype reported here. To achieve this, additional aspects such as the management of product gas bubbles within the percolator, which are expected to become increasingly relevant at higher conversion rates, should be addressed through appropriate larger-scale electrolyser design. Nevertheless, given the sub-millibar precision of GDE pressure differential setting demonstrated here, it is expected that the FFE design can enable the vertical scale-up of the EC-CO_2R technology, as achieved in industrial chlor-alkali electrolysers.

4 Experimental

4.1 Materials and chemicals

Electrolytes were composed of 1 M potassium hydrogen carbonate (99.5+%, Thermo Fisher Scientific) which was prepared using ultrapure deionised water (18.2 MΩ cm,

Merck Milli-Q). Gas diffusion layers (SGL Carbon – Sigracet 28BC and Freudenberg – H15C13) and anionic exchange membrane (PiperION®, self-Supporting 80 μm, Versogen) were purchased from the Fuel Cell Store (Tygrave Enterprises Ltd.). Silver nanopowder catalyst (20–40 nm, 99.9%) was purchased from Thermo Fisher Scientific and mixed with Nafion® D-520 dispersion (5% w/w in water and 1-propanol. Tygrave Enterprises Ltd.) used as a binder and ion-transport medium. Catalyst inks (for 34 × 3 cm^2 electrode area) were prepared as a mixture of 600 mg silver nanopowder, 2 g Nafion® resin, 20 g ultrapure deionised water and 20 g isopropanol (Reagent grade, Fisher Scientific). The mixtures were sonicated for 20 min using an ultrasonic probe (Cole Parmer) before spray-coating onto the microporous layer side of GDLs by use of an airbrush (Gaahleri GHPM-Mobius TG) using 2 bar compressed air. Electrodes of size 5 × 5 cm^2 were prepared by use of a proportional ink mixture. Catalyst loadings were estimated as geometric averages and all samples were on average 1.1 ± 0.3 mg cm^{-2} (Table S1). Polypropylene (PP) geotextile (0.8 mm thickness) and polyurethane (PU) open-cell foam (5.0 mm thickness) were procured from a local textile distributor. Nickel foam (99.99% for battery cathode substrate) was purchased from Cambridge Energy Solutions Ltd. and used as anode for sacrificial oxygen evolution reaction. A silver–silver chloride reference electrode (3 M KCl) was purchased from BASi.

4.2 Cell designs

Custom designed H-S and electrolysis cells and reservoirs were manufactured in-house and constructed from transparent acrylic. Full schematics and engineering drawings are provided for reproduction of all designs used (see the SI). Silicone gaskets of variable thickness were used for controlling component compression and sealing each design. For percolator testing, a H-S cell was used, featuring a chamber for a 40 × 5 cm^2 area percolator of variable thickness, and pressure sampling points every 5 cm. For threshold pressure measurements, a modified 2-chamber flow cell was employed with a 3.16 × 3.16 cm^2 electrode area. For percolated FFE EC-CO_2R experiments, a 32 × 1 cm^2 electrochemical electrode area was used, paired with a nickel foam anode and PiperION® membrane. A 3D-printed flow frame in differing thicknesses was used featuring multiple pressure sampling points. Conductive copper adhesive tape was used for the cathodic and anodic current collectors for connection to the potentiostat.

4.3 Electrolyte and CO_2 circulation

Electrolyte was circulated through the cells by either pumping using a 4-roller peristaltic pump (WP1000, Welco Co. Ltd.) or gear pump (MGD1000, TCS Micropumps), or gravity-fed from height-adjusted reservoirs. The flow rate of gravity-fed electrolytes was unrestricted and instead determined by the architecture of the system. In all cases, electrolyte was circulated using perfluoroalkoxy alkane tubing with an internal 1/8″ diameter. Electrolyte flow rates were measured by use of a floating-ball flow meter (0 to 200 mL min^{-1} range) or by the prior calibration of the pumps as a function of voltage.

CO_2 gas (99.9%, British Oxygen Company Ltd.) was flowed through the cells using perfluoroalkoxy alkane tubing with an internal 1/16″ diameter. Flow rates were controlled and measured using digital mass flow controllers and meters supplied by Alicat Scientific. A CO_2 reactant flow rate of 100 mL min^{-1} was flowed through the cells during experiments. An additional CO_2 purge flow rate of 200 to 400 mL min^{-1} was flowed through the catholyte chamber headspace during electrolysis experiments. The combined flow was used for overcoming the backpressure of the gas chromatograph inlet for online analysis. Flow diagrams are provided for clarity (see the SI).

4.4 Electrolysis

Electrochemical experiments were controlled using an IVIUMstat potentiostat with a 10 A, 4 V range. Cell resistances were measured by use of EIS under non-flowing conditions in the range of 1 MHz to 0.1 Hz with a 10 mV amplitude at −1 V cell voltage. The intercept of the Nyquist plot real axis was recorded for cell resistances without EIS equivalent-circuit fitting.

4.5 Product quantification

Products from electrolysis were identified and quantified by gas chromatography (GC) for gaseous phase products. Liquid phase products were not analysed or quantified in this work due to the high quantitative yield of the Ag catalyst for gaseous products. The GC employed (Agilent 7820A) was configured with 30 m length, 0.53 mm diameter PLOT/Q and MOLSIEVE columns in series for hydrocarbon and small molecule separation, respectively. The instrument was equipped with a methaniser catalyst and flame ionisation detector for CO, and a thermal conductivity detector for H_2 quantification. The instrument was pre-calibrated within the range of ≈100 to 10 000 ppm by dilutions of bespoke 1 and 0.1% calibration gasses supplied by British Oxygen Company Ltd. The dilutions were prepared by use of a custom built pressure vessel constructed from Swagelok fittings, and concentrations were calculated based upon pressure ratios (see the SI). Samples were introduced into the GC by direct connection of the electrolyser outlet to the GC sample loop inlet, and GC runs were performed approximately every 25 minutes.

Author contributions

Craig Armstrong: investigation, methodology, data curation, visualisation, formal analysis, writing – original draft preparation, writing – review & editing. Bjørnar Sandnes: methodology, software, writing – review & editing. Enrico Andreoli: conceptualisation, validation, resources,

supervision, project administration, funding acquisition, writing – review & editing.

Conflicts of interest

There are no conflicts to declare.

Data availability

The data supporting this article have been included as part of the supplementary information (SI).

Supplementary information: additional experimental methods and results are available online. See DOI: https://doi.org/10.1039/d5im00372e.

Acknowledgements

Support was provided by the UK Engineering and Physical Sciences Research Council through the SUSTAIN Manufacturing Hub EP/S018107/1, and by Research Wales Innovation Fund through a Collaboration Booster Grant. The authors would also like to thank the Swansea University mechanical engineering workshop for their assistance in producing cell and reservoir designs. Gratitude is also extended to Shekina Anand-Bhoopalan, Dr Bill Gannon and Dr James Courtney for assistance with laboratory activities.

References

1 M. Mikkelsen, M. Jørgensen and F. C. Krebs, The teraton challenge. a review of fixation and transformation of carbon dioxide, *Energy Environ. Sci.*, 2010, **3**, 43–81.
2 P. De Luna, C. Hahn, D. Higgins, S. A. Jaffer, T. F. Jaramillo and E. H. Sargent, What would it take for renewably powered electrosynthesis to displace petrochemical processes?, *Science*, 2019, **364**, 350.
3 A. Ozden, F. P. García de Arquer, J. E. Huang, J. Wicks, J. Sisler, R. K. Miao, C. P. O'Brien, G. Lee, X. Wang, A. H. Ip, E. H. Sargent and D. Sinton, Carbon-efficient carbon dioxide electrolysers, *Nat. Sustain.*, 2022, **5**, 563–573.
4 R. J. Detz, C. J. Ferchaud, A. J. Kalkman, J. Kemper, C. Sánchez-Martínez, M. Saric and M. V. Shinde, Electrochemical CO_2 conversion technologies: State-of-the-art and future perspectives, *Sustainable Energy Fuels*, 2023, **7**, 5445–5472.
5 M. Tayyab, M. Dreis, D. Blaudszun, K. Pellumbi, U. Nzotcha, H. Tempel, M. Q. Masood, H. Weinrich, S. Stießel, K. junge Puring, R. A. Eichel and U. P. Apfel, Closing the carbon cycle: Challenges and opportunities of CO_2 electrolyser designs in light of cross-industrial CO_2 source-sink matching in the european landscape, *Energy Environ. Sci.*, 2025, **18**, 6854–6873.
6 R. G. Grim, Z. Huang, M. T. Guarnieri, J. R. Ferrell, L. Tao and J. A. Schaidle, Transforming the carbon economy: Challenges and opportunities in the convergence of low-cost electricity and reductive CO_2 utilization, *Energy Environ. Sci.*, 2020, **13**, 472–494.
7 A. Mustafa, B. G. Lougou, Y. Shuai, Z. Wang and H. Tan, Current technology development for CO_2 utilization into solar fuels and chemicals: A review, *J. Energy Chem.*, 2020, **49**, 96–123.
8 S. Nitopi, E. Bertheussen, S. B. Scott, X. Liu, A. K. Engstfeld, S. Horch, B. Seger, I. E. L. Stephens, K. Chan, C. Hahn, J. K. Nørskov, T. F. Jaramillo and I. Chorkendorff, Progress and perspectives of electrochemical CO_2 reduction on copper in aqueous electrolyte, *Chem. Rev.*, 2019, **119**, 7610–7672.
9 D. R. Kauffman, J. Thakkar, R. Siva, C. Matranga, P. R. Ohodnicki, C. Zeng and R. Jin, Efficient electrochemical CO_2 conversion powered by renewable energy, *ACS Appl. Mater. Interfaces*, 2015, **7**, 15626–15632.
10 B. Belsa, L. Xia and F. P. García de Arquer, CO_2 electrolysis technologies: Bridging the gap toward scale-up and commercialization, *ACS Energy Lett.*, 2024, **9**, 4293–4305.
11 T. Burdyny and W. A. Smith, CO_2 reduction on gas-diffusion electrodes and why catalytic performance must be assessed at commercially-relevant conditions, *Energy Environ. Sci.*, 2019, **12**, 1442–1453.
12 H. Shin, K. U. Hansen and F. Jiao, Techno-economic assessment of low-temperature carbon dioxide electrolysis, *Nat. Sustain.*, 2021, **4**, 911–919.
13 Z. Ni, H. Liang, Z. Yi, R. Guo, C. Liu, Y. Liu, H. Sun and X. Liu, Research progress of electrochemical CO_2 reduction for copper-based catalysts to multicarbon products, *Coord. Chem. Rev.*, 2021, **441**, 213983.
14 S. Ahn, K. Klyukin, R. J. Wakeham, J. A. Rudd, A. R. Lewis, S. Alexander, F. Carla, V. Alexandrov and E. Andreoli, Poly-amide modified copper foam electrodes for enhanced electrochemical reduction of carbon dioxide, *ACS Catal.*, 2018, **8**, 4132–4142.
15 T. Yan, X. Chen, L. Kumari, J. Lin, M. Li, Q. Fan, H. Chi, T. J. Meyer, S. Zhang and X. Ma, Multiscale CO_2 electrocatalysis to C2+ products: Reaction mechanisms, catalyst design, and device fabrication, *Chem. Rev.*, 2023, **17**, 10530–10583.
16 M. Jun, J. Kundu, D. H. Kim, M. Kim, D. Kim, K. Lee and S. Il Choi, Strategies to modulate the copper oxidation state toward selective C2+ production in the electrochemical CO_2 reduction reaction, *Adv. Mater.*, 2024, **36**, 2313028.
17 J. Liu, P. Li, J. Bi, Q. Zhu and B. Han, Design and preparation of electrocatalysts by electrodeposition for CO_2 reduction, *Chem. – Eur. J.*, 2022, **28**, e202200242.
18 E. Andreoli, CO_2-to-ethylene electroreduction gets a boost, *Nat. Catal.*, 2021, **4**, 8–9.
19 X. Chen, J. Chen, N. M. Alghoraibi, D. A. Henckel, R. Zhang, U. O. Nwabara, K. E. Madsen, P. J. A. Kenis, S. C. Zimmerman and A. A. Gewirth, Electrochemical CO_2-to-ethylene conversion on polyamine-incorporated cu electrodes, *Nat. Catal.*, 2021, **4**, 20–27.
20 S. Hernandez-Aldave and E. Andreoli, Fundamentals of gas diffusion electrodes and electrolysers for carbon dioxide utilisation: Challenges and opportunities, *Catalysis*, 2020, **10**, 1–34.
21 M. Ma, E. L. Clark, K. T. Therkildsen, S. Dalsgaard, I. Chorkendorff and B. Seger, Insights into the carbon balance for CO_2 electroreduction on cu using gas diffusion electrode reactor designs, *Energy Environ. Sci.*, 2020, **13**, 977–985.

22 H. Rabiee, L. Ge, X. Zhang, S. Hu, M. Li and Z. Yuan, Gas diffusion electrodes (GDEs) for electrochemical reduction of carbon dioxide, carbon monoxide, and dinitrogen to value-added products: A review, *Energy Environ. Sci.*, 2021, **14**, 1959–2008.

23 J. Na, B. Seo, J. Kim, C. W. Lee, H. Lee, Y. J. Hwang, B. K. Min, D. K. Lee, H. S. Oh and U. Lee, General technoeconomic analysis for electrochemical coproduction coupling carbon dioxide reduction with organic oxidation, *Nat. Commun.*, 2019, **10**, 5193.

24 D. Tian, Z. Qu and J. Zhang, Electrochemical condition optimization and techno-economic analysis on the direct CO_2 electroreduction of flue gas, *Appl. Energy*, 2023, **351**, 121787.

25 I. Bagemihl, L. Cammann, M. Pérez-Fortes, V. van Steijn and J. R. van Ommen, Techno-economic assessment of CO_2 electrolysis: How interdependencies between model variables propagate across different modelling scales, *ACS Sustainable Chem. Eng.*, 2023, **11**, 10130–10141.

26 S. Park, D. T. Wijaya, J. Na and C. W. Lee, Towards the large-scale electrochemical reduction of carbon dioxide, *Catalysts*, 2021, **11**, 1–30.

27 R. L. Cook, R. C. MacDuff and A. F. Sammells, High rate gas phase CO_2 reduction to ethylene and methane using gas diffusion electrodes, *J. Electrochem. Soc.*, 1990, **137**, 607–608.

28 D. Higgins, C. Hahn, C. Xiang, T. F. Jaramillo and A. Z. Weber, Gas-diffusion electrodes for carbon dioxide reduction: A new paradigm, *ACS Energy Lett.*, 2019, **4**, 317–324.

29 P. Wang, H. Yang, C. Tang, Y. Wu, Y. Zheng, T. Cheng, K. Davey, X. Huang and S. Z. Qiao, Boosting electrocatalytic CO_2–to–ethanol production via asymmetric C–C coupling, *Nat. Commun.*, 2022, **13**, 3754.

30 J. Albo and A. Irabien, Cu_2O-loaded gas diffusion electrodes for the continuous electrochemical reduction of CO_2 to methanol, *J. Catal.*, 2016, **343**, 232–239.

31 A. Senocrate, F. Bernasconi, D. Rentsch, K. Kraft, M. Trottmann, A. Wichser, D. Bleiner and C. Battaglia, Importance of substrate pore size and wetting behaviour in gas diffusion electrodes for CO_2 reduction, *ACS Appl. Energy Mater.*, 2022, **5**, 14504–14512.

32 T. N. Nguyen and C. T. Dinh, Gas diffusion electrode design for electrochemical carbon dioxide reduction, *Chem. Soc. Rev.*, 2020, **49**, 7488–7504.

33 L. M. Baumgartner, C. I. Koopman, A. Forner-Cuenca and D. A. Vermaas, Narrow pressure stability window of gas diffusion electrodes limits the scale-up of CO_2 electrolyzers, *ACS Sustainable Chem. Eng.*, 2022, **10**, 4683–4693.

34 A. A. Samu, I. Szenti, Á. Kukovecz, B. Endrődi and C. Janáky, Systematic screening of gas diffusion layers for high performance CO_2 electrolysis, *Commun. Chem.*, 2023, **6**, 41.

35 J. A. Abarca, G. Díaz-Sainz, I. Merino-Garcia, G. Beobide, J. Albo and A. Irabien, Optimized manufacturing of gas diffusion electrodes for CO_2 electroreduction with automatic spray pyrolysis, *J. Environ. Chem. Eng.*, 2023, **11**, 109724.

36 L. Li, J. Chen, V. S. S. Mosali, Y. Liang, A. M. Bond, Q. Gu and J. Zhang, Hydrophobicity graded gas diffusion layer for stable electrochemical reduction of CO_2, *Angew. Chem., Int. Ed.*, 2022, **61**, e202208534.

37 P. Gyenes, A. A. Samu, D. Hursán, V. Józó, A. Serfőző, B. Endrődi and C. Janáky, Flooding revisited: Electrolyte management ensures robust electrochemical CO_2 reduction, *Energy Environ. Sci.*, 2025, **18**, 7124–7135.

38 M. E. Leonard, L. E. Clarke, A. Forner-Cuenca, S. M. Brown and F. R. Brushett, Investigating electrode flooding in a flowing electrolyte, gas-fed carbon dioxide electrolyzer, *ChemSusChem*, 2020, **13**, 400–411.

39 D. Wakerley, S. Lamaison, J. Wicks, A. Clemens, J. Feaster, D. Corral, S. A. Jaffer, A. Sarkar, M. Fontecave, E. B. Duoss, S. Baker, E. H. Sargent, T. F. Jaramillo and C. Hahn, Gas diffusion electrodes, reactor designs and key metrics of low-temperature CO_2 electrolysers, *Nat. Energy*, 2022, **7**, 130–143.

40 H. Rabiee, B. Ma, Y. Yang, F. Li, P. Yan, Y. Wu, X. Zhang, S. Hu, H. Wang, L. Ge and Z. Zhu, Advances and challenges of carbon-free gas-diffusion electrodes (GDEs) for electrochemical CO_2 reduction, *Adv. Funct. Mater.*, 2025, **35**, 2411195.

41 M. K. Kovalev, H. Ren, M. Zakir Muhamad, J. W. Ager and A. A. Lapkin, Minor product polymerization causes failure of high-current CO_2-to-ethylene electrolyzers, *ACS Energy Lett.*, 2022, **7**, 599–601.

42 P. Jeanty, C. Scherer, E. Magori, K. Wiesner-Fleischer, O. Hinrichsen and M. Fleischer, Upscaling and continuous operation of electrochemical CO_2 to co conversion in aqueous solutions on silver gas diffusion electrodes, *J. CO2 Util.*, 2018, **24**, 454–462.

43 S. Hernandez-Aldave and E. Andreoli, Oxygen depolarised cathode as a learning platform for CO_2 gas diffusion electrodes, *Catal. Sci. Technol.*, 2022, **12**, 3412–3420.

44 I. Moussallem, J. Jörissen, U. Kunz, S. Pinnow and T. Turek, Chlor-alkali electrolysis with oxygen depolarized cathodes: History, present status and future prospects, *J. Appl. Electrochem.*, 2008, **38**, 1177–1194.

45 I. Moussallem, S. Pinnow, N. Wagner and T. Turek, Development of high-performance silver-based gas-diffusion electrodes for chlor-alkali electrolysis with oxygen depolarized cathodes, *Chem. Eng. Process.*, 2012, **52**, 125–131.

46 M. Ma, E. L. Clark, K. T. Therkildsen, S. Dalsgaard, I. Chorkendorff and B. Seger, Insights into the carbon balance for CO_2 electroreduction on Cu using gas diffusion electrode reactor designs, *Energy Environ. Sci.*, 2020, **13**, 977–985.

47 Y. Hori, Electrochemical CO_2 reduction on metal electrodes, in *Modern Aspects of Electrochemistry*, ed. C. G. Vayenas, R. E. White and M. E. Gamboa-Aldeco, Springer New York, New York, 2008, pp. 89–189.

48 C. H. Lee, B. Zhao, J. K. Lee, K. F. Fahy, K. Krause and A. Bazylak, Bubble formation in the electrolyte triggers voltage instability in CO_2 electrolyzers, *iScience*, 2020, **23**, 101094.

49 M. Großeheide, D. Schaffeld, R. Keller and M. Wessling, A falling film design for electrochemical CO_2 reduction, *Electrochem. Commun.*, 2023, **150**, 107487.

50 K. Xie, R. K. Miao, A. Ozden, S. Liu, Z. Chen, C. Dinh, J. E. Huang, Q. Xu, C. M. Gabardo, G. Lee, J. P. Edwards, C. P. O. Brien, S. W. Boettcher, D. Sinton and E. H. Sargent, Bipolar membrane electrolyzers enable high single-pass CO_2 electroreduction to multicarbon products, *Nat. Commun.*, 2022, **13**, 3609.

51 B. De Mot, J. Hereijgers, N. Daems and T. Breugelmans, Insight in the behavior of bipolar membrane equipped carbon dioxide electrolyzers at low electrolyte flowrates, *Chem. Eng. J.*, 2022, **428**, 131170.

52 K. Yang, R. Kas, W. A. Smith and T. Burdyny, Role of the carbon-based gas diffusion layer on flooding in a gas diffusion electrode cell for electrochemical CO_2 reduction, *ACS Energy Lett.*, 2021, **6**, 33–40.

53 K. Liu, W. A. Smith and T. Burdyny, Introductory guide to assembling and operating gas diffusion electrodes for electrochemical CO_2 reduction, *ACS Energy Lett.*, 2019, **4**, 639–643.

54 G. M. Homsy, Viscous fingering in porous media, *Annu. Rev. Fluid Mech.*, 1987, **19**, 271–311.

55 D. Zhang, J. M. Campbell, J. A. Eriksen, E. G. Flekkøy, K. J. Måløy, C. W. MacMinn and B. Sandnes, Frictional fluid instabilities shaped by viscous forces, *Nat. Commun.*, 2023, **14**, 3044.

56 R. Lenormand, E. Touboul and C. Zarcone, Numerical models and experiments on immiscible displacements in porous media, *J. Fluid Mech.*, 1988, **189**, 165–187.

57 G. Faita and F. Erico, *Eur. Pat.*, WO2003042430A2, 2003.

58 G. Faita, *Eur. Pat.*, WO2008009661A2, 2008.

59 G. Damian Polcyn, N. Bredemeyer, C. Roosen, D. Donst, P. Toros, P. Woltering, D. Hoormann, W. an der Lippe, P. Hofmann, S. Köberle, F. Funck, W. Stolp and B. Langanke, *US Pat.*, US9680172B2, 2017.

60 Z. Kowalczuk and M. S. Tatara, Improved model of isothermal and incompressible fluid flow in pipelines versus the darcy-weisbach equation and the issue of friction factor, *J. Fluid Mech.*, 2020, **891**, A5.

61 R. J. Charbeneau, *Groundwater Hydraulics and Pollutant Transport*, Waveland Pr Inc, 2006.

62 J. H. Chun, D. H. Jo, S. G. Kim, S. H. Park, C. H. Lee and S. H. Kim, Improvement of the mechanical durability of micro porous layer in a proton exchange membrane fuel cell by elimination of surface cracks, *Renewable Energy*, 2012, **48**, 35–41.

63 H. Markötter, J. Haußmann, R. Alink, C. Tötzke, T. Arlt, M. Klages, H. Riesemeier, J. Scholta, D. Gerteisen, J. Banhart and I. Manke, Influence of cracks in the microporous layer on the water distribution in a PEM fuel cell investigated by synchrotron radiography, *Electrochem. Commun.*, 2013, **34**, 22–24.

64 Y. Kong, M. Liu, H. Hu, Y. Hou, S. Vesztergom, M. de J. Gálvez-Vázquez, I. Zelocualtecatl Montiel, V. Kolivoška and P. Broekmann, Cracks as efficient tools to mitigate flooding in gas diffusion electrodes used for the electrochemical reduction of carbon dioxide, *Small Methods*, 2022, **6**, 2200369.

65 M. E. Leonard, M. J. Orella, N. Aiello, Y. Román-Leshkov, A. Forner-Cuenca and F. R. Brushett, Editors' choice—Flooded by success: On the role of electrode wettability in CO_2 electrolyzers that generate liquid products, *J. Electrochem. Soc.*, 2020, **167**, 124521.

66 C. M. Gabardo, A. Seifitokaldani, J. P. Edwards, C. T. Dinh, T. Burdyny, M. G. Kibria, C. P. O'Brien, E. H. Sargent and D. Sinton, Combined high alkalinity and pressurization enable efficient CO_2 electroreduction to CO, *Energy Environ. Sci.*, 2018, **11**, 2531–2539.

67 J. P. Edwards, Y. Xu, C. M. Gabardo, C. T. Dinh, J. Li, Z. B. Qi, A. Ozden, E. H. Sargent and D. Sinton, Efficient electrocatalytic conversion of carbon dioxide in a low-resistance pressurized alkaline electrolyzer, *Appl. Energy*, 2020, **261**, 114305.

68 C.-T. Dinh, T. Burdyny, M. G. Kibria, A. Seifitokaldani, C. M. Gabardo, F. Pelayo García De Arquer, A. Kiani, J. P. Edwards, P. De Luna, O. S. Bushuyev, C. Zou, R. Quintero-Bermudez, Y. Pang, D. Sinton and E. H. Sargent, CO_2 electroreduction to ethylene via hydroxide-mediated copper catalysis at an abrupt interface, *Science*, 2018, **360**, 783–787.

69 F. Bidault, D. J. L. Brett, P. H. Middleton and N. P. Brandon, Review of gas diffusion cathodes for alkaline fuel cells, *J. Power Sources*, 2009, **187**(1), 39–48.

70 P. Gouérec, L. Poletto, J. Denizot, E. Sanchez-Cortezon and J. H. Miners, The evolution of the performance of alkaline fuel cells with circulating electrolyte, *J. Power Sources*, 2004, **129**, 193–204.

71 G. Liu, D. McLaughlin, S. Thiele and C. Van Pham, Correlating catalyst ink design and catalyst layer fabrication with electrochemical CO_2 reduction performance, *Chem. Eng. J.*, 2023, **460**, 141757.

72 R. Wang, H. Haspel, A. Pustovarenko, A. Dikhtiarenko, A. Russkikh, G. Shterk, D. Osadchii, S. Ould-Chikh, M. Ma, W. A. Smith, K. Takanabe, F. Kapteijn and J. Gascon, Maximizing Ag utilization in high-rate CO_2 electrochemical reduction with a coordination polymer-mediated gas diffusion electrode, *ACS Energy Lett.*, 2019, **4**, 2024–2031.

73 C. T. Dinh, F. P. García De Arquer, D. Sinton and E. H. Sargent, High rate, selective, and stable electroreduction of CO_2 to CO in basic and neutral media, *ACS Energy Lett.*, 2018, **3**, 2835–2840.

74 S. S. Bhargava, F. Proietto, D. Azmoodeh, E. R. Cofell, D. A. Henckel, S. Verma, C. J. Brooks, A. A. Gewirth and P. J. A. Kenis, System design rules for intensifying the electrochemical reduction of CO_2 to CO on Ag nanoparticles, *ChemElectroChem*, 2020, **7**, 2001–2011.

75 Y. S. Ham, Y. S. Park, A. Jo, J. H. Jang, S. K. Kim and J. J. Kim, Proton-exchange membrane CO_2 electrolyzer for CO production using Ag catalyst directly electrodeposited onto gas diffusion layer, *J. Power Sources*, 2019, **437**, 226898.

76 S. Ma, R. Luo, J. I. Gold, A. Z. Yu, B. Kim and P. J. A. Kenis, Carbon nanotube containing Ag catalyst layers for efficient and selective reduction of carbon dioxide, *J. Mater. Chem. A*, 2016, **4**, 8573–8578.

77 S. Ma, R. Luo, S. Moniri, Y. Lan and P. J. A. Kenis, Efficient electrochemical flow system with improved anode for the conversion of CO_2 to CO, *J. Electrochem. Soc.*, 2014, **161**, F1124–F1131.
78 L. Li, J. Wen, T. W. B. Lo, J. Yin and Q. Lei, Wettability-controlled electrocatalytic carbon dioxide reduction, *Chem.: Methods*, 2025, **5**, e202400080.
79 J. Disch, L. Bohn, L. Metzler and S. Vierrath, Strategies for the mitigation of salt precipitation in zero-gap CO_2 electrolyzers producing CO, *J. Mater. Chem. A*, 2023, **11**, 7344–7357.
80 Y. Xu, J. P. Edwards, S. Liu, R. K. Miao, J. E. Huang, C. M. Gabardo, C. P. O'Brien, J. Li, E. H. Sargent and D. Sinton, Self-cleaning CO_2 reduction systems: Unsteady electrochemical forcing enables stability, *ACS Energy Lett.*, 2021, **6**, 809–815.